Preprints.org

Article

Not peer-reviewed version

CFD-Based Performance Analysis of Hybrid MWCNTs–SiO_2 Nanofluids in Plate Heat Exchangers: Enhancing Heat Transfer with Minimal Pressure Drop

Saeed Zeinali Heris *, Nima Zolfagharian, Seyed Borhan Mousavi *, Shamin Hosseini Nami

Posted Date: 21 August 2024

doi: 10.20944/preprints202408.1412.v1

Keywords: Thermal conductivity; Convective heat transfer; Pressure drop; Nusselt number; Reynolds number; Heat exchanger

Preprints.org is a free multidiscipline platform providing preprint service that is dedicated to making early versions of research outputs permanently available and citable. Preprints posted at Preprints.org appear in Web of Science, Crossref, Google Scholar, Scilit, Europe PMC.

Copyright: This is an open access article distributed under the Creative Commons Attribution License which permits unrestricted use, distribution, and reproduction in any medium, provided the original work is properly cited.

Preprints.org (www.preprints.org) | NOT PEER-REVIEWED | Posted: 21 August 2024 doi:10.20944/preprints202408.1412.v1

Disclaimer/Publisher's Note: The statements, opinions, and data contained in all publications are solely those of the individual author(s) and contributor(s) and not of MDPI and/or the editor(s). MDPI and/or the editor(s) disclaim responsibility for any injury to people or property resulting from any ideas, methods, instructions, or products referred to in the content.

Article

CFD-Based Performance Analysis of Hybrid MWCNTs–SiO_2 Nanofluids in Plate Heat Exchangers: Enhancing Heat Transfer with Minimal Pressure Drop

Saeed Zeinali Heris [1,2,*], Nima Zolfagharian [2], Seyed Borhan Mousavi [3,*] and Shamin Hosseini Nami [4]

[1] School of Safety Science & Engineering, Xi'an University of Science and Technology, 58, Yanta Mid. Rd., Xi'an, Shaanxi, China 710054
[2] Faculty of Chemical and Petroleum Engineering, University of Tabriz, Tabriz, Iran
[3] J. Mike Walker '66 Mechanical Engineering Department, Texas A&M University, College Station, TX 77843, USA
[4] School of Chemical, Biological and Materials Engineering, The University of Oklahoma, Norman, Oklahoma 73019, USA
* Correspondence: sz.heris@xust.edu.cn; seyedborhanm@gmail.com, borhanm@tamu.edu

Abstract: Heat exchangers play a vital role in numerous sectors like power generation and automotive manufacturing. Enhancing the energy efficiency of these exchangers stands as a significant hurdle. Utilizing nanofluids emerges as an optimal solution to augment heat transfer rates, leveraging their superior thermal conductivity while addressing economic constraints linked with traditional heat exchanger technologies. The motivation for this study is to consider the comprehensive synergistic features of MWCNTs, SiO_2, and hybrid MWCNTs–SiO_2 EG-based nanofluids in plate heat exchangers. This was achieved by simulating a plate heat exchanger using CFD (Fluent and Gambit softwares) considering the comparison of two SiO_2, MWCNTs, and their hybrid forms at different mass concentrations. The Reynolds-Averaged Navier-Stokes (RANS) method was employed to model turbulent flows, and the nanoparticles were compared in both single-phase and two-phase states, with their properties derived from experimental studies. Moreover, Nusselt number, convective heat transfer coefficient, and pressure drop variations were computed at different Reynolds numbers. The findings indicated an increase in the Nusselt number with the incorporation of the hybrid nanofluid, achieving a maximum enhancement of 11.19% in comparison to EG at a Reynolds number of 240 and a concentration of 0.86 wt.%. Noticeably, the pressure drop remained negligible at lower Reynolds numbers, exhibiting marginal variations up to 0.3% at higher Reynolds numbers. At a concentration of 0.86 wt.% and a Reynolds number of 480, the introduction of MWCNTs, hybrid, and SiO_2 nano-additives resulted in respective increases in the heat transfer coefficient by 21.02%, 10.76%, and 2.16% and corresponding alterations in pressure drop of 0.11%, 0.04%, and 0.02%.

Keywords: Thermal conductivity; Convective heat transfer; Pressure drop; Nusselt number; Reynolds number; Heat exchanger

1. Introduction

Thermal pollution arises when the heat generated by industrial activities, electronic devices, and vehicles is released into the atmosphere, posing a threat to marine ecosystems. Utilizing heat exchangers and appropriate cooling agents can facilitate the retrieval of this dispersed heat. It is crucial to carefully choose the most suitable heat exchanger configuration and cooling medium to efficiently recover waste heat energy [1, 2]. Plate heat exchangers are widely employed for heat transfer between hot and cold fluids. These exchangers utilize thin metal plates arranged in a specific

© 2024 by the author(s). Distributed under a Creative Commons CC BY license.

Preprints.org (www.preprints.org) | NOT PEER-REVIEWED | Posted: 21 August 2024 doi:10.20944/preprints202408.1412.v1

pattern, inducing flow turbulence and enhancing heat transfer efficiency. The design involves multiple thin plates aligned to create space between them, with one pipe for cold fluid and another for hot fluid. Heat transfer occurs through the plate walls between the fluids, resulting in increased efficiency. Due to their effectiveness, plate heat exchangers are extensively utilized across various industries [3].

Various efforts have been undertaken to enhance heat transfer efficiency and reduce transfer time in heat exchangers. Recent advancements in nanotechnology have facilitated these improvements. Typically, heat transfer enhancement involves modifying the design, often through blade adjustments [4]. Moreover, enhancing the thermal properties of heat transfer fluids can also increase heat transfer within heat exchangers [5-8]. Zheng et al. [9] investigated the impact of nanofluids (Al_2O_3, SiC, CuO, and Fe_3O_4) on water in a plate heat exchanger at varying mass fractions (0.05, 0.1, 0.5, and 1%). They found that at a mass fraction of 1% and volume flows ranging from 3 to 9 L/min, the heat transfer rate increased by 21.9% compared to pure water. Additionally, they developed an experimental model for the Nusselt number based on their findings. Ajeeb et al. [10] conducted an experimental study on a plate heat exchanger utilizing Al_2O_3 nanofluids prepared at various low concentrations (0.01, 0.05, 0.10, 0.15, and 0.20 vol%) in combination with base fluids including distilled water and a mixture of distilled water with ethylene glycol (15 and 30% ethylene glycol). The experiments covered a range of flow rates from 0.03 to 0.093 l/s. The findings revealed that increasing the concentration of nanoparticles led to improved heat transfer, reaching a maximum enhancement of 27% with a 0.2 vol% concentration of Al_2O_3 in distilled water, albeit accompanied by an 8% rise in pressure drop. However, the heat transfer enhancement diminished with higher proportions of ethylene glycol, with a maximum enhancement of 19.1% observed at 0.2 vol% for Al_2O_3 nanofluid with 30% ethylene glycol.

Many researchers recommend using hybrid nanofluids in plate heat exchangers to enhance performance compared to conventional nanofluids. Hybrid nanofluids, by integrating diverse nanoparticles like metal oxides and carbon nanotubes into the base fluid, typically demonstrate superior thermal conductivity compared to traditional nanofluids [11-23]. This incorporation leads to significant enhancements in thermal properties. Additionally, the interaction between different nanoparticles within hybrid nanofluids can generate synergistic effects, further improving dispersion, stability, and heat transfer characteristics [24-29]. Moreover, hybrid nanofluids exhibit reduced tendencies for particle agglomeration and sedimentation in contrast to conventional nanofluids [30-35]. Bhattad et al. [36] examined hybrid nanofluids consisting of Al_2O_3–MWCNT/water on a corrugated plate heat exchanger. They explored different volume ratios (5:0, 4:1, 3:2, 2:3, 1:4, and 0:5) with a volume fraction of 0.01%, operating within a flow rate of 2 to 4 L per minute and coolant temperatures ranging from 10 to 25 ◦C. Their results demonstrated a notable 15.2% improvement in the heat transfer coefficient. Sundar et al. [37] evaluated the efficiency and number of transfer units of a plate heat exchanger utilizing Fe_3O_4–SiO_2/Water hybrid nanofluids. Their findings demonstrated that the introduction of hybrid nanofluids resulted in increased plate heat exchanger effectiveness and number of transfer units. Furthermore, these parameters were further enhanced with higher flow rates of nanofluids. Specifically, with a 1.0% volume of nanofluid in the plate heat exchanger, effectiveness and number of transfer units increased by 13.23% and 24.51%, respectively, at a Reynolds number of 571.9 compared to using water alone. Afshari et al. [38] conducted an experimental study on the heat transfer characteristics of a plate heat exchanger containing 8, 12, and 16 plates. They used TiO_2/water and TiO_2–Al_2O_3/water hybrid nanofluids at a 1 wt.% concentration. Their results showed that the TiO_2–Al_2O_3/water hybrid nanofluid exhibited superior heat transfer rates compared to the TiO_2/water nanofluid. Additionally, they observed a respective increase in the heat transfer coefficient of 7.5%, 9.6%, and 12.3% with 8, 12, and 16 plates when using the TiO_2–Al_2O_3/water nanofluid.

After acknowledging the beneficial impact of nanofluids on improving the thermal performance of plate heat exchangers and recognizing the effectiveness of hybrid nanofluids, limited research has been conducted in this area. Previous studies predominantly focused on Al_2O_3 or TiO_2 hybrids, neglecting the consideration of MWCNTs–SiO_2 hybrid nanofluids. Additionally, there is a lack of

Preprints.org (www.preprints.org) | NOT PEER-REVIEWED | Posted: 21 August 2024 doi:10.20944/preprints202408.1412.v1

comparison between the effects of individual nanoparticles and hybrid ones in the literature. Thus, for the first time, we not only investigated MWCNTs, SiO_2, and MWCNTs–SiO_2 hybrid nanofluids in the heat transfer properties of plate heat exchangers but also examined and validated a comprehensive range of influential parameters in this study.

Thus, in this evaluation, a plate heat exchanger was simulated using computational fluid dynamics with Fluent and Gambit softwares. The system and nanofluid properties were determined through user-defined functions (UDFs) and a C++ program. Ethylene glycol (EG) served as the base fluid, with nanoparticles including SiO_2, MWCNTs, and a hybrid combination. The Reynolds-Averaged Navier-Stokes (RANS) method was employed to model turbulent flows, and the nanoparticles were compared in both single-phase and two-phase (mixture model) states. Nusselt number, convective heat transfer coefficient, and pressure drop variations were computed for Reynolds numbers of 60, 120, 180, 240, and 480, and concentrations of 0, 0.11, 0.26, 0.47, 0.62, and 0.86 wt.%.

2. Numerical Approaches

2.1. Geometry and Mesh Optimization

In this investigation, the plate heat exchanger (PHE) underwent simulation and numerical analysis based on computational fluid dynamics (CFD) using Fluent software (Fluent v19.2) and the geometric model was meticulously fashioned using Gambit v2.4.6. In order to determine the thermophysical properties of the nanofluid under consideration and to save time and costs, user-defined functions (UDFs) and coding in the C++ programming environment were utilized. Each individual plate within the system was compartmentalized into four channels, equally distributed between the cold and hot sides, as depicted in Figure 1. Notably, the port effect was systematically considered across all examined scenarios. The meshing of plates was executed using an automated approach for both the inlet and outlet ports. Hexahedral elements were employed to intricately mesh the inner and outer walls, ensuring precision in the meshing process.

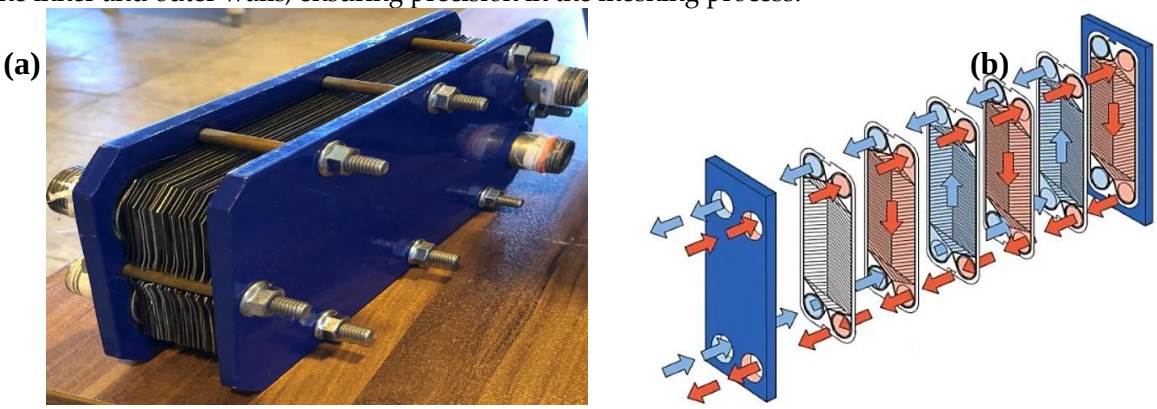

Figure 1. (a) Experimental PHE, (b) schematic for counter-current flow mechanism of PHE (obtained from [39]).

The PHE under examination belongs to the gasketed plate type, featuring plates arranged in a compact configuration and separated by gaskets. These gaskets play a pivotal role that extends beyond simple sealing between the plates; they serve the dual purpose of directing the flow of hot and cold fluid streams. Consequently, this functionality prevents the commingling of these distinct fluid streams, ensuring a discrete and controlled heat exchange within the inter-plate spacing. The specifications of the plate heat exchanger utilized in this study are documented in Table 1. As observed in Figure 1(a), the specified PHE was designed with a configuration comprising four pipes. This arrangement included two inlet pipes for the hot fluid, one outlet pipe for the cold fluid, and two additional inlet pipes for the cold fluid, complemented by one outlet pipe for the hot fluid. The external shell of the heat exchanger, in conjunction with the internal plates, played a crucial role in

Preprints.org (www.preprints.org) | NOT PEER-REVIEWED | Posted: 21 August 2024 doi:10.20944/preprints202408.1412.v1

enhancing heat transfer. As a result, both the geometry production and the primary mesh of the heat exchanger shell were meticulously modelled.

Table 1. Physical characteristics of PHE.

Parameters	Values
Number of plates (N)	21
Length of plates (L)	220 mm
Width of plates (w)	80 mm
Thickness of plates (t)	0.05 mm
Channel diameter (D)	19.2 mm
Depth of plates (b_c)	1.5 mm
Plate area enlargement factor (ϕ)	1.23

2.2. Governing Equations and Methods

For the ease of numerical simulation in Fluent, it is essential to apply simplifying assumptions based on the specified conditions. For this research, the following assumptions were adopted to streamline the numerical solution process while aligning with the specific conditions and objectives of the study:

- The fluid flow was three-dimensional and incompressible.
- The flow was steady.
- The nanofluid under investigation was examined in both single-phase and two-phase states.
- Consideration was not given to the effects of sedimentation on heat transfer.
- The flow was assumed to be turbulent in nature.

For the evaluation of key performance parameters in the heat exchanger, calculations were conducted for Reynolds number (Re), Nusselt number (Nu), heat transfer coefficient (h_h), apparent fluid velocity (U_s) in accordance with equations (1-5) [40-43]. Parameters ρ, μ, $\dot{V}$, N, and D_e denote the density, viscosity, volumetric flow rate of the fluid, number of flow passages, and equivalent diameter.

$$Re = \frac{\rho U_s D_e}{\mu} \quad (1)$$

$$U_s = \frac{\dot{V}}{W b_c N} \quad (2)$$

$$D_e = 2b_c \quad (3)$$

$$u = \frac{h_h D_e}{k} \quad (4)$$

$$h_h = \frac{Q_{avg}}{A(T_{h,b} - T_{w,h})} \quad (5)$$

In the simulation of multiphase nanofluids, careful consideration is essential for the accurate representation of the physical properties of both the base fluid and nanoparticles. These properties include density, viscosity, constant-pressure specific heat, and thermal conductivity. It is crucial to acknowledge the inherent distinction between the relationships governing the physical properties of substances in the mixture flow model and those specifically applicable to nanofluids. In the current

Preprints.org (www.preprints.org) | NOT PEER-REVIEWED | Posted: 21 August 2024 doi:10.20944/preprints202408.1412.v1

numerical simulation employing Fluent software and a multiphase mixture model, a systematic approach was imperative to establish a correlation between the properties of nanofluids and the applied mixture model. Fundamentally, the properties of the base fluid and nanoparticles require a configuration that harmonizes them with the equations of the mixture flow model. Termed "equivalencing" of physical properties, this process ensures a smooth integration of these properties into the mixture model equations, ultimately achieving alignment with the properties specified for nanofluids in referenced articles. This equivalencing involves the adaptation of properties to harmonize with the mixture flow model equations, effectively transforming them into equivalent properties. It is important to highlight that user-defined functions (UDFs) play a crucial role in implementing these equivalences, facilitating the integration of formulated relationships derived from various reference articles. Default relationships for the physical properties of nanofluids in a multiphase mixture model were expressed as follows, where φ, C_P, and K stands for particle volume concentration, specific heat, and conductivity of the fluid, respectively [44-47].

$$\rho_{mix} = (1-\varphi)\rho_1 + \varphi\rho_2 \quad (6)$$

$$(C_P)_{mix} = (1-\varphi)(C_P)_1 + \varphi(C_P)_2 \quad (7)$$

$$\mu_{mix} = (1-\varphi)\mu_1 + \varphi\mu_2 \quad (8)$$

$$K_{mix} = (1-\varphi)k_1 + \varphi k_2 \quad (9)$$

In the present study, the simulation of the targeted nanofluid was conducted in both single-phase and two-phase (mixture model) states. These simulations aim to comprehensively capture the behavior of the nanofluid, considering different phases, and analyze the corresponding fluid dynamics and heat transfer characteristics. The formulation, outlining the mathematical representation of the governing equations for both the single-phase and mixture models, is presented in Table 2 [48-51]. V/v, P, and τ represent the velocity, pressure, and shear stress, correspondingly. Moreover, symbols of λ, and T/t, a, and H represent the thermal conductivity of the fluid, temperature, acceleration, and enthalpy, sequentially. The t, m, k, f, p, and r subscripts stand for turbulent, mixture, k^{th} phase, primary phase, particle property, and nanofluid/base-fluid ratio, respectively. Compression work and viscous dissipation were considered negligible in the energy equations 15 and 25. Equation 19 in the momentum conservation incorporated $\vec{V}_{dr,k}$, representing the drift velocity for the secondary phase k (i.e., nanoparticles in this study). The slip velocity, denoting the velocity of the secondary phase (p) relative to the velocity of the primary phase (f), was a crucial parameter in this context. The determination of the relative velocity was based on equation 22 as proposed by Manninen et al. [49], while the calculation of the drag function utilized equation 23 by Schiller and Naumann [50].

Table 2. Governing equations for both the single–phase and mixture models.

Single phase:		
Conservation of mass	$\nabla.\left(\rho_m\vec{V}\right) = 0,$	(10)
	$\rho_m = \sum_{i=1}^{N} \varphi_i\rho_i$	(11)
Conservation of momentum	$\nabla.\left(\rho_m\vec{V}\vec{V}\right) = -\nabla P + \nabla.(\tau - \tau_t)$	(12)
	$\tau = \mu_m\nabla\vec{V}_m$	(13)

Preprints.org (www.preprints.org) | NOT PEER-REVIEWED | Posted: 21 August 2024 doi:10.20944/preprints202408.1412.v1

$$\tau_t = \sum_{k=1}^{n} \varphi_k \rho_k \overline{v_k v_k} \quad (14)$$

Conservation of energy

$$\nabla.\left(\rho \vec{V} C_p T\right) = \nabla.\left(\lambda \nabla T - C_p \rho_m \overline{vt}\right) \quad (15)$$

Two-phase (mixture model):

Conservation of mass

$$\nabla.\left(\rho_m \vec{V}_m\right) = 0 \quad (16)$$

$$\vec{V}_m = \frac{\sum_{i=1}^{N} \varphi_i \rho_i \vec{V}_i}{\rho_m} \quad (17)$$

Conservation of momentum

$$\nabla.\left(\rho_m \vec{V}_m \vec{V}_m\right) = -\nabla P_m + \nabla.(\tau - \tau_t) + \nabla.\left(\sum_{k=1}^{n} \varphi_k \rho_k \vec{V}_{dr,k} \vec{V}_{dr,k}\right) \quad (18)$$

$$\vec{V}_{dr,k} = \vec{V}_k - \vec{V}_m, \quad \vec{V}_{pf} = \vec{V}_p - \vec{V}_F \quad (19)$$

Volume fraction

$$\nabla.\left(\varphi_p \rho_p \vec{V}_m\right) = -\nabla.\left(\varphi_p \rho_p \vec{V}_{dr,p}\right) \quad (20)$$

Drift velocity

$$\vec{V}_{dr,p} = \vec{V}_{pf} - \sum_{k=1}^{n} \frac{\varphi_k \rho_k}{\rho_m} \vec{V}_{fk} \quad (21)$$

Slip/Relative velocity

$$\vec{V}_{pf} = \frac{\rho_p d_p^2}{\mu_f f_{drag} 18} \frac{(\rho_p - \rho_m)}{\rho_p} a \quad (22)$$

Drag function

$$f_{drag} = \begin{cases} 0.0183 Re_p & Re_p > 1000 \\ 1 + 0.15 Re_p^{0.687} & Re_p < 1000 \end{cases} \quad (23)$$

Acceleration

$$a = g - (\vec{V}_m.\nabla)\vec{V}_m \quad (24)$$

Conservation of energy

$$\nabla.\left(\sum_{k=1}^{n} \varphi_k \vec{V}_k \left(\rho_k H_k + P\right)\right) = \nabla.\left(\lambda \nabla T - C_p \rho_m \overline{vt}\right) \quad (25)$$

The thermophysical properties of nanofluids including density, viscosity, thermal conductivity, and resistance were studied. For modelling nanofluids, whether in a single-phase or two-phase state, it is necessary to formulate relationships for each parameter. Generalized expressions for each property exist, but they can vary based on the physics of the problem and the governing conditions, including the type of nanoparticles and base fluid, as well as the desired thermal conductivity and viscosity. Experimental research has provided various relationships, specifically for thermal conductivity and viscosity, based on the empirical findings of different articles that investigated the nanoparticles under consideration in this study. For expressing the thermal conductivity based on the concentration of nanofluid and temperature equation 26 was used based on literature [52]. Subscripts of bf and nf indicate the base fluid and nanofluid, respectively.

Preprints.org (www.preprints.org) | NOT PEER-REVIEWED | Posted: 21 August 2024 doi:10.20944/preprints202408.1412.v1

$$\frac{k_{nf}}{k_{bf}} = 0.905 + 0.002069\varphi T + 0.04375\varphi^{0.09265}T^{0.3305}0.0063\varphi^{3} \quad (26)$$

Equation 27, was employed for definition of viscosity (Pa.s) based on shear rate (γ) in reciprocal seconds (1/s) [53].

$$\mu_{nf} = 15.88\varphi^{0.8514}T^{-1.189}\gamma^{-0.5639} \quad (27)$$

Equation 28 provides the density of nanofluids in a general form [54], considering the general case and assuming a single nanoparticle type. Nevertheless, in the study at hand, the nanoparticle was addressed in a hybrid form (hnf), leading to the adoption of equation 29 [55].

$$\rho_{nf} = \varphi\rho_{np} + (1-\varphi)\rho_{bf} \quad (28)$$

$$\rho_{hnf} = \varphi_{np1}\rho_{np1} + \varphi_{np2}\rho_{np2} + \left(1-\varphi_{np1}-\varphi_{np2}\right)\rho_{bf} \quad (29)$$

Similar to the relationship for nanofluid density, Pak and colleagues [54] provided an expression for the specific heat in the case of a single nanoparticle type:

$$C_{p,nf} = \frac{\varphi\rho_{np}C_{p,np}+(1-\varphi)\rho_{bf}C_{p,bf}}{\rho_{nf}}) \quad (30)$$

Meanwhile, Tekabi et al. [55] have extended the above relationship for hybrid nanofluids:

$$C_{p,nf} = \frac{\varphi\rho_{np}C_{p,np}+(1-\varphi)\rho_{bf}C_{p,bf}}{\rho_{nf}}) \quad (31)$$

2.3. Turbulence Model

For turbulent flows, the RANS (Reynolds-Averaged Navier-Stokes) method stands out as the predominant simulation technique. In this approach, the initial step involved formulating the Reynolds-averaged Navier-Stokes equations. Following the averaging process, the Reynolds stresses, representing unknowns in the equations, were then simulated using a turbulence model. The velocity and pressure terms can be decomposed into mean and fluctuating components as expressed in equation 32-33.

$$u = \bar{u} + u',\ \bar{u} = \frac{1}{t}\int_0^t u dt \quad (32)$$

$$p = \bar{p} + \acute{p} \quad (33)$$

Here, the terms $\bar{u}$ and $\bar{p}$ represent the mean velocity and pressure, while u' and $\acute{p}$ represent the fluctuating velocity and pressure components. By substituting the velocity terms into the continuity equation and performing the averaging, we obtain the following averaged continuity equation:

$$\frac{\partial}{\partial x_i}(\bar{u}_i) = 0 \quad (34)$$

If these equations were written for momentum in the z, y, and x directions and finally substituted into equation 8, the Reynolds-averaged Navier-Stokes equation can be obtained:

$$\frac{\partial(\rho\bar{u}_i)}{\partial t} + \frac{\partial\left(\rho\bar{u}_i\bar{u}_j\right)}{\partial x} = -\frac{\partial\bar{p}}{\partial x_i} + \frac{\partial}{\partial x_i}\left[\mu\left(\frac{\partial\bar{u}_i}{\partial x_j} + \frac{\partial\bar{u}_j}{\partial x_i} - \frac{2}{3}\delta_{ij}\frac{\partial\bar{u}_m}{\partial x_m}\right)\right] + \frac{\partial}{\partial x_i}\left(-\rho\overline{\acute{u}_i\acute{u}_j}\right) \quad (35)$$

The quantity $\left(-\rho\overline{\acute{u}_i\acute{u}_j}\right)$ is identified as the Reynolds stress tensor, representing a symmetric tensor. The primary distinction between equations for steady and turbulent flows was found in the Reynolds stress tensor term. Overall, this term characterized momentum exchange and was not a stress tensor; instead, it originated from momentum considerations. In 1877, Boussinesq introduced the hypothesis that equated Reynolds stresses (shear stresses in the vortex direction) to the product of turbulent viscosity and velocity gradients. The equation can be formulated as follows:

Preprints.org (www.preprints.org) | NOT PEER-REVIEWED | Posted: 21 August 2024 doi:10.20944/preprints202408.1412.v1

$$\left(-\rho\overline{\acute{u}_i\acute{u}_j}\right) = \mu_t\left(\frac{\partial \bar{u}_i}{\partial x_j} + \frac{\partial \bar{u}_j}{\partial x_i}\right) - \frac{2}{3}\delta_{ij}\left(\rho k + \mu_t\frac{\partial \bar{u}_m}{\partial x_m}\right) \quad (36)$$

The aforementioned equations are known as the RANS (Reynolds-Averaged Navier-Stokes) equations, which are explicit equations and do not rely on any simplifying assumptions to be derived. Consequently, these equations did not form a closed system since the number of unknowns exceeded the available information. To solve these equations, the Reynolds stresses needed to be modelled. Thus, in this research, considering the prevailing conditions of the turbulent flow issue, computational costs, the physical laws governing the flow, and the investigation of the multiscale nature of the nanoparticle in question, the Realizable k-ε model was used. This approach excels in handling flows with adverse gradients or separation, outperforming other models. Additionally, it accurately captures the expansion of swirling and surface flows [56, 57].

2.4. Properties of Nanofluid

As reiterated before, the focus of this research involves the hybrid simulation of silicon oxide nanoparticles (SiO_2) and multi-walled carbon nanotubes (MWCNTs) as nano additives in ethylene glycol (EG), as base fluid. To this end thermophysical properties for the base fluid, at various temperatures are presented in Table 3 and physical specifications of the targeted nanoparticles and EG are provided in Table 4.

Table 3. Thermophysical properties of EG [58].

Temperature (°C)	Density (kg/m³)	Specific heat (kJ/kg·K)	Kinematic viscosity (m²/s)	Thermal conductivity (W/m·K)
0	1130.75	2.294	7.53×10^{-6}	0.242
20	1116.65	2.382	1.92×10^{-5}	0.249
40	1101.43	2.474	8.69×10^{-6}	0.256
60	1087.66	2.562	4.75×10^{-6}	0.260
80	1077.56	2.650	2.98×10^{-6}	0.261
100	1058.50	2.742	2.03×10^{-6}	0.263

Table 4. Physical specifications of SiO_2 nanoparticles, MWCNTs, EG, and water at 30 °C.

Material	Thermal conductivity (W/m·K)	Electrical conductivity (S/m)	Density (kg/m³)	Diameter (nm)	Ref.
SiO_2	1.38	10^{-21}	2220	20–30	[59]
MWCNTs	1500–3000	>0.1	2100	Outer :20–50 Inner: 2–6	[52]
EG	0.615	6	999	–	[59]
Water	0.252	1.07	1110	–	[59]

3. Results and Discussion

3.1. Geometric Model

As illustrated in Figure 1, the geometry of PHE involves placing multiple plates in a stacked arrangement, which were separated from each other by gaskets. As observed in Figure 2a, for heat exchange in the specified PHE, two streams of hot and cold fluids were defined in the Fluent software

Preprints.org (www.preprints.org) | NOT PEER-REVIEWED | Posted: 21 August 2024 doi:10.20944/preprints202408.1412.v1

according to the diagram. The cold stream, with a temperature of 22.4 °C, entered from the bottom of the heat exchanger and exited from the top, maintaining a pressure of 101325 Pa (1 atm). The hot stream, with a temperature of 50.5 °C, entered from the top of the heat exchanger, and after heat exchange with the cold stream at a constant pressure (1 atm), exited from the bottom. In the assessment of heat transfer parameters and pressure drop, hybrid nanoparticles were introduced into the fluid stream at a concentration of 0.86 wt.%. The Reynolds number under investigation spanned from 60 to 480. As stated in section 2.1, Gambit was employed for domain blocking and mesh generation in this research. As depicted in Figure 2b-c, the blocking process was based on the selection of appropriate points and the subsequent generation of lines, surfaces, and ultimately volumes. This procedure was established not only for mesh lines but also for mesh surfaces and volumes. The intended mesh was of hexahedral type with a structured arrangement, cast on the geometric blocks, forming a network with an organized structure. Additionally, for more accurate prediction and precise solution of the governing equations of the flow, near the walls of the flow surfaces, a boundary layer mesh has been utilized.

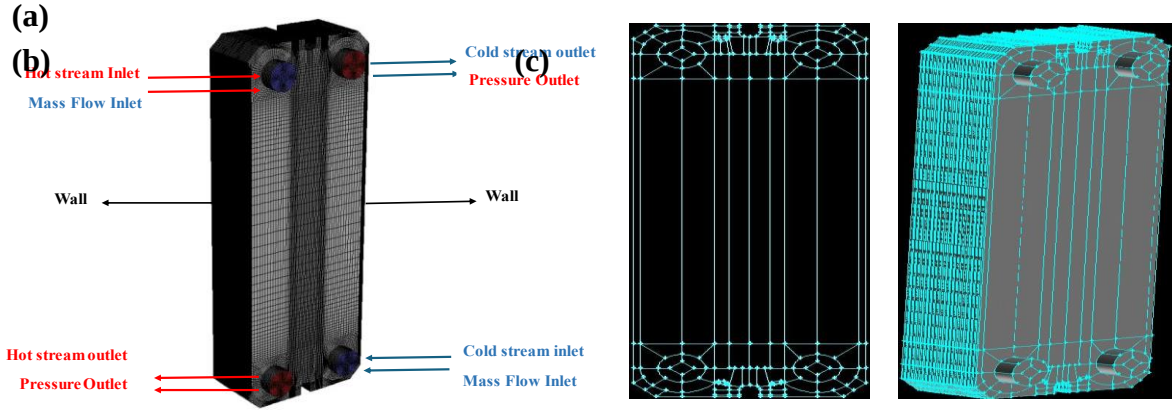

Figure 2. (a) The computational domain and boundary conditions in Ansys Fluent 19.4, computational domain mesh (b) 2–D, and (c) 3–D.

3.2. Solver Settings and Boundary Conditions

In this study, the governing equations underwent resolution in an incompressible and transient fashion employing the finite volume method. Given the low fluid velocity, the resolution of the problem employed a pressure-based solver. This solver facilitated the acquisition of the velocity field through the solution of momentum equations. The pressure field, on the other hand, was ascertained by addressing the pressure correction equation derived through the manipulation of continuity and momentum equations. To augment the precision of the results, advanced discretization methods of higher order were deployed throughout the simulation. For pressure-velocity coupling, gradient, and pressure equations coupled, cell-based least squares, and second order solutions were applied, respectively. While the second order upwind method was used for solving momentum, turbulent kinetic energy, turbulent dissipation rate, and energy equations.

The method applied to the momentum and energy equations for grid discretization involved a second-order accuracy. Furthermore, a second-order algorithm was utilized for pressure calculation. Calculations were carried out with accuracy up to 10^{-6} for all equations. To achieve desirable convergence with fewer iterations, a coupled algorithm was used to couple the velocity and pressure equations for steady-state solutions. In transient simulations, this method provides accurate and comprehensive solutions for large time steps. In contrast to the segregated approach, the coupled solution method simultaneously solves a set of coupled momentum equations and pressure-based continuity equations, eliminating the need for solving a pressure correction equation. Following the simultaneous solution of pressure and velocity fields, the remaining equations, such as the energy equation, were solved separately as in the previous method. The Coupled method allows for simultaneous convergence of pressure and velocity equations, enhancing the convergence of the

Preprints.org (www.preprints.org) | NOT PEER-REVIEWED | Posted: 21 August 2024 doi:10.20944/preprints202408.1412.v1

problem; However, it occupies more memory, approximately 3.1 times more, compared to the segregated approach. The boundary conditions governing the problem were determined according to Table 5. The relaxation factor for pressure and momentum was set at 0.5, while for turbulent kinetic energy, turbulent dissipation rate, and energy, was adjusted to 0.75. Density, body forces, and turbulent viscosity were individually set to a value of 1.

Table 5. The boundary conditions governing the problem.

Boundary name	Boundary type	Value
Cold stream inlet	Mass flow inlet	$\dot{M}$ =4 L/min
		T=22.4 °C
Hot stream inlet	Mass flow inlet	$\dot{M}$=3.28 L/min
		T=50.5 °C
Hot stream outlet	Pressure Outlet	P=101325 Pa
Cold stream outlet	Pressure Outlet	P=101325 Pa
Intermediate walls	Wall	Coupled, Nonslip (U=0.0, V =0.0)
Outer walls	Wall	Q=0.0 w/m^2, Nonslip (U=0.0, V =0.0)

3.3. Grid Independence

Ensuring that the numerical solution results remain consistent regardless of the computational grid is a crucial first step in any numerical simulation. The objective was consistency in results, regardless of the mesh employed. To evaluate this independence, an initial coarse mesh was generated, initiating the simulation. A selected variable underwent scrutiny to examine mesh independence. Subsequently, a finer mesh with an increased number of cells was utilized, and the results were compared with those from the initial stage. If changes proved negligible, the initial coarse mesh was deemed optimal. In instances of significant changes, a finer mesh was reintroduced, and the results were compared to the preceding stage. This iterative process persisted until the mesh achieved the desired fineness, resulting in minor or constant changes with an increased number of cells. Thus, a network with an optimal cell count for numerical simulation was identified. Furthermore, the network had to adhere to standard criteria, encompassing aspect ratio, orthogonality quality, skewness, etc. The augmentation of network cells should not compromise overall network quality. Figure 3a-b illustrates quality contours of the network, with corresponding data specifying aspect ratio, orthogonal quality, and cell equiangular skewness values at 1.000-25.000, 0.367-1.000, and 0.000-0.774, respectively.

Preprints.org (www.preprints.org) | NOT PEER-REVIEWED | Posted: 21 August 2024 doi:10.20944/preprints202408.1412.v1

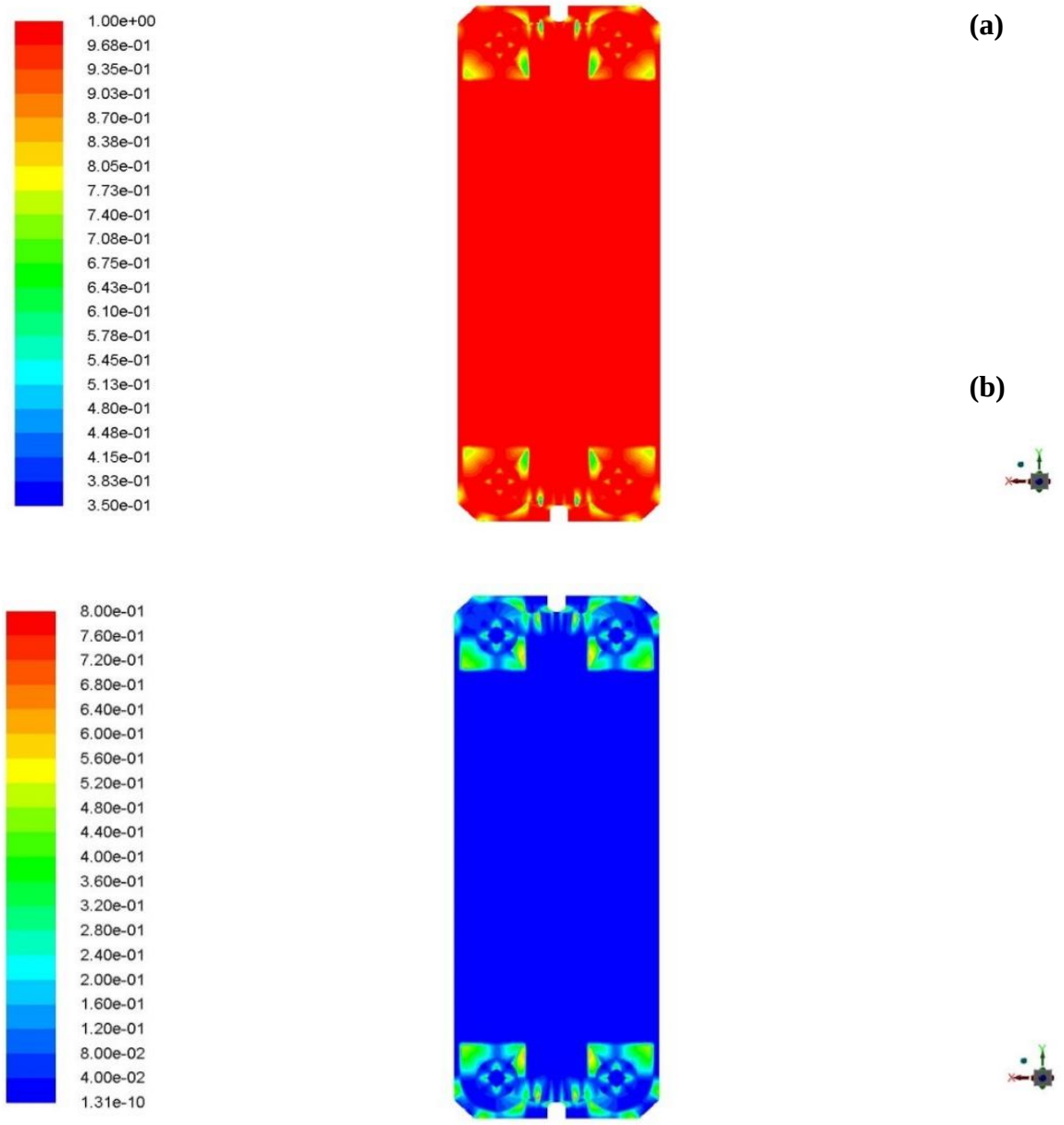

Figure 3. Contour plots of mesh quality for (a) orthogonal quality, and (b) skewness.

As depicted in Figure 3a, the orthogonal quality parameter showcased the degree of orthogonality quality among cells in the network, with values spanning from zero to one. A proximity to one signified heightened orthogonality and quality, whereas values nearing zero indicated diminished orthogonality. Furthermore, it was apparent that within the central regions of the designated network, where the most substantial heat transfer occurred, the values of this parameter approached one, signifying an exemplary level of network quality. This observation reinforces the notion of superior network performance in regions critical to heat transfer within the specified network. The skewness parameter ranged between zero and one, indicating the grid skewness. A value of zero corresponded to excellent grid quality when the angles of the nodal elements were in degrees, and as the angles became sharper, the value approached one. Non-compliance with this criterion significantly affected the accuracy of the solution, leading to errors in the diffusion term. As observed in Figure 3b, the skewness parameter in heat transfer-sensitive areas, namely the central regions, exhibited values close to zero, signifying excellent network quality. Other areas, including the inlet and outlet channels, also showed values inclined towards zero, depicting an acceptable description of network quality in these regions.

Preprints.org (www.preprints.org) | NOT PEER-REVIEWED | Posted: 21 August 2024 doi:10.20944/preprints202408.1412.v1

To assess mesh independence in the numerical results for the heat exchanger, an initial coarse mesh of 311,748 cells was generated, and outlet temperatures for the hot and cold streams were acquired. Subsequently, the cell count was approximately doubled to 749,418 cells. The noticeable slope in the temperature change diagram at the hot outlet prompted an increase in the mesh cell count to around 1,159,080 (approximately 1.6 million). In this scenario, the temperature changes at the outlets of both hot and cold streams in both models remained significant. The mesh cell count was further increased to nearly 1.75 million (1,749,930), maintaining a high slope in the temperature changes at the cold outlet for both models. However, the slope of temperature changes decreased concerning the number of cells in the computational mesh for the hot stream, indicating an approach to an optimal mesh. Subsequently, the mesh cell count reached the maximum examined value, i.e., 3.5 million (3,457,801). In this case, the temperature changes at the outlets of both hot and cold streams for both models became negligible. Consequently, the mesh with 3.5 million cells was deemed suitable for further simulation. Although the mesh with 3.5 million cells provided more accurate numerical results, 1.75 million cells had significantly less computational time and was more economic with an acceptable accuracy. The investigation of mesh independence is presented in Table 6, categorized into two based on the outlet temperatures of the cold and hot streams into two distinct cases.

Table 6. The examined cases for mesh independence.

Category Number	Inlet hot stream temperature (°C)	outlet hot stream temperature (°C)	Inlet cold stream temperature (°C)	outlet cold stream temperature (°C)	Hot stream flow rate (L/min)	Cold stream flow rate (L/min)
1	50.5	43.53	22.4	29.38	4	3.28
2	60	46.75	22.4	29.87	2.26	4

In Figure 4a-b and Figure 4c-d, the examination of grid independence is illustrated for the first and second states, specifically focusing on the outlet temperature of both the cold and hot streams. The depicted results in Figure 4a-d reveal negligible differences in the outlet temperature, leading to the selection of 1.75 million cells for the subsequent phases of the study.

Preprints.org (www.preprints.org) | NOT PEER-REVIEWED | Posted: 21 August 2024 doi:10.20944/preprints202408.1412.v1

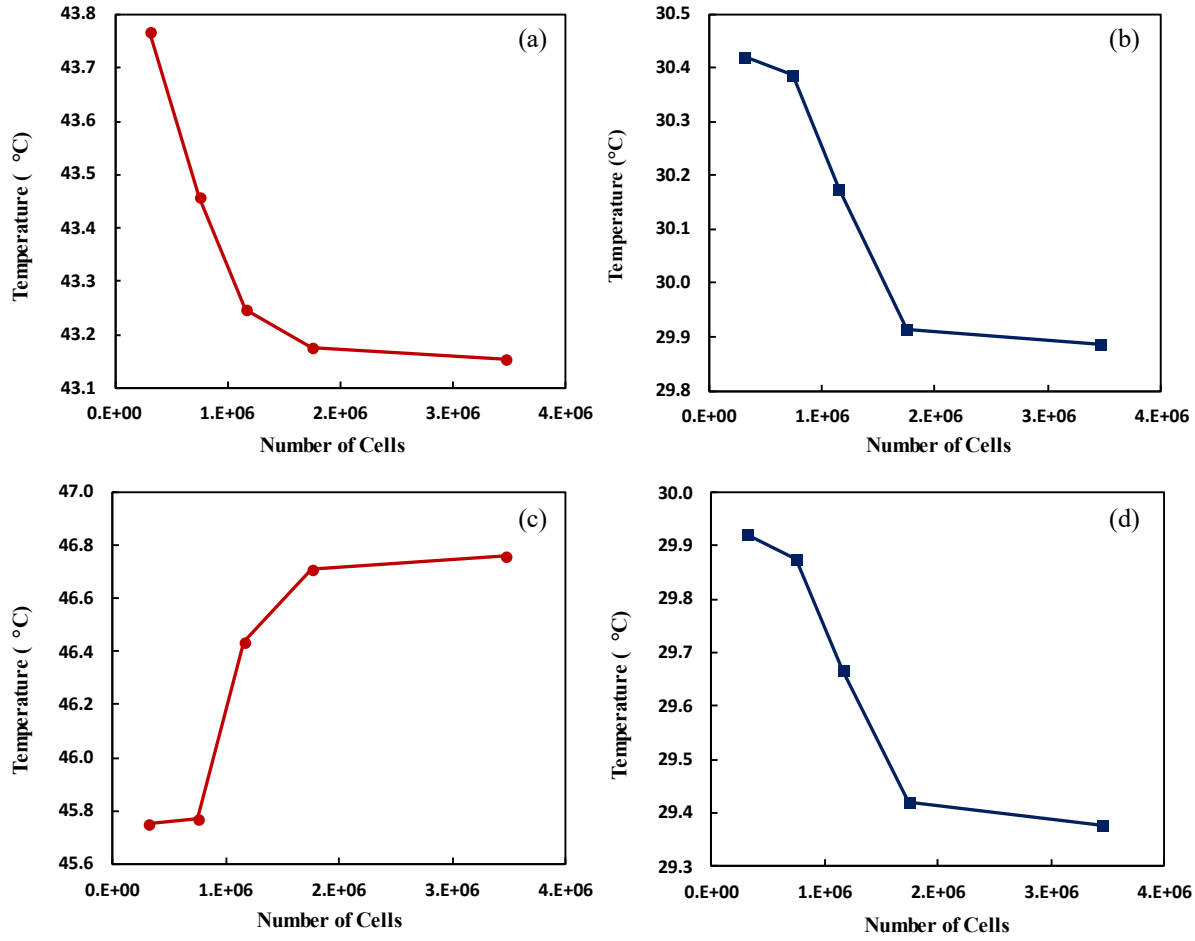

Figure 4. Grid independence of outlet temperature of first state (a) hot stream, (b) cold stream, and second state (c) hot stream, (d) cold stream.

3.4. Model Validation

Validation of numerical methods in computational fluid dynamics is essential to ensure the precision of the chosen computational approach. Typically, this involves comparing numerical results with experimental data. However, the reliability of this comparison hinges on the close alignment of the experimental model with the numerical research model. In this study, validation was conducted based on the research by Abbasi et al. [60], carried out within our research group. The geometric parameters employed were consistent with those in the referenced research, with a focus on carboxyl and hydroxyl-functionalized nanoparticles. For this specific validation, non-slip conditions were applied to the carboxyl-functionalized MWCNTs at a volumetric fraction of 0.3%, as illustrated in Figure 5. The simulation results exhibited a high degree of concordance with experimental findings, affirming the precision of the numerical solution.

Preprints.org (www.preprints.org) | NOT PEER-REVIEWED | Posted: 21 August 2024 doi:10.20944/preprints202408.1412.v1

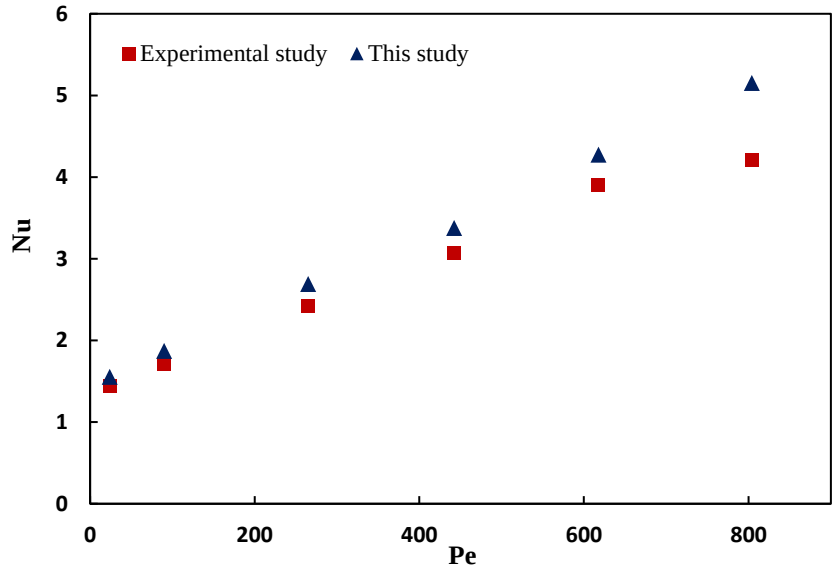

Figure 5. Variations of Nusselt numbers as a function of Peclet number (simulation and experimental data).

3.5. Thermophysical Properties

Following the model verification, our investigation advanced towards its primary objective: examining the impact of hybrid SiO_2-MWCNTs presence in EG on heat transfer and pressure drop within an experimental geometry. The outcomes derived from simulations under both single-phase and two-phase conditions were detailed. The convective heat transfer coefficient (h), Nusselt number (Nu), and pressure drop (Δp) emerged as the central subjects of discussion and analysis in this study.

Variations of the Nusselt number as a function of hybrid nanoparticle concentration corresponding to Reynolds numbers of 60, 120, 180, 240, and 480 are illustrated in Figure 6. To account for limitations in the concentration of the specified nanoparticle in the equations governing its thermophysical properties, specifically the thermal conductivity coefficient, a concentration composition ranging from 0 to 0.86 wt.% was considered. The results revealed a positive correlation between the Nusselt number and the concentration of hybrid nanoparticles. Additionally, at constant concentration, an increase in the Reynolds number led to a higher Nusselt number. For instance, at a concentration of 0.26 wt.%, the Nusselt number values were 10.18, 13.89, 16.93, 16.57, and 27.52 at Reynolds numbers of 60, 120, 180, 240, and 480, respectively. Furthermore, the escalation of the Reynolds number induced a transition to more turbulent flow, diminishing fluid accumulation and stagnation. This turbulent flow played a crucial role in augmenting the Nusselt number, particularly at higher concentrations and Reynolds numbers. The Reynolds number, representing fluid velocity within the channels, was expressed as a non-dimensionalized flow rate in numerical methods. Hence, the justification for the observed relationship between the Nusselt number and the Reynolds number was grounded in the fluid dynamics principles. Notably, the highest Nusselt number for a concentration of 0.86 wt.% was achieved at a Reynolds number of 480, registering a 10.76% increase compared to the base fluid.

Similar trends were identified in a study conducted by Bazdar et al. [61], where the Nusselt number demonstrated an increase with rising Reynolds numbers and volume fractions of nanoparticles. The enhancement in heat transfer can be justified by the introduction of nanoparticles, resulting in a concurrent increase in the conductive heat transfer coefficient and a reduction in the specific heat capacity of the base fluid. This phenomenon underscored the improved thermal performance observed in the system. The addition of nanoparticles contributed to heightened conductive heat transfer coefficients within the fluid medium. The presence of these nanoparticles facilitated more efficient heat conduction through the medium, promoting an overall enhancement in thermal conductivity. Simultaneously, the reduction in the specific heat capacity of the base fluid

Preprints.org (www.preprints.org) | NOT PEER-REVIEWED | Posted: 21 August 2024 doi:10.20944/preprints202408.1412.v1

further increased the heat transfer efficiency. With a decreased specific heat capacity, the fluid required less energy to undergo temperature changes, thereby promoting more effective and rapid heat transfer processes.

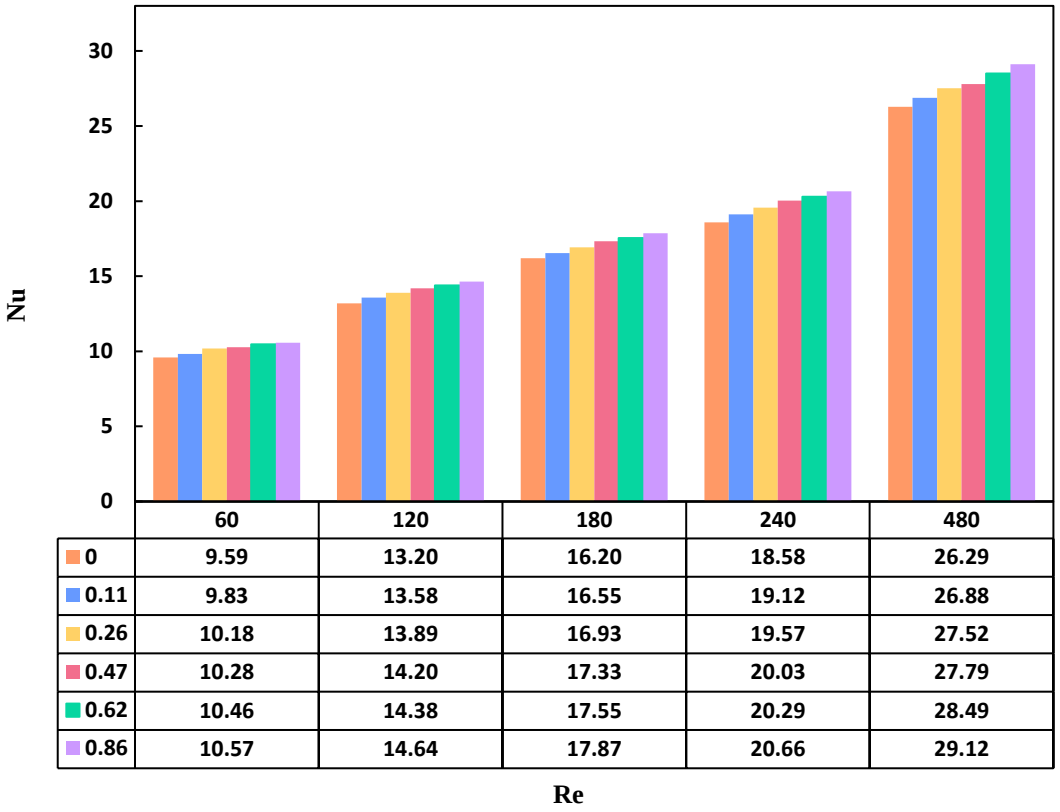

	60	120	180	240	480
0	9.59	13.20	16.20	18.58	26.29
0.11	9.83	13.58	16.55	19.12	26.88
0.26	10.18	13.89	16.93	19.57	27.52
0.47	10.28	14.20	17.33	20.03	27.79
0.62	10.46	14.38	17.55	20.29	28.49
0.86	10.57	14.64	17.87	20.66	29.12

Figure 6. Variations of Nusselt number at different Reynolds numbers and concentrations.

Investigating the effect of nanoparticle concentration (ranging from 0 to 0.86 wt.%) on the convective heat transfer coefficient at different Reynolds numbers (240, 180, 120, 60, and 480) revealed intriguing insights, as illustrated in Figure 7. Upon analyzing the obtained results alongside equations 27 and 32, a clear direct correlation emerged between the convective heat transfer coefficient, the Nusselt number, and consequently, the Reynolds number. Notably, the variations in the convective heat transfer coefficient demonstrated an increasing trend with higher concentrations. This phenomenon can be attributed to the heightened thermal conductivity exhibited by nanofluids in comparison to the base fluid. Additionally, the proportional relationship between thermal conductivity and the heat transfer coefficient further emphasized this trend [62]. To illustrate, at a consistent Reynolds number of 60, the heat transfer coefficient for the base fluid, nanofluid with 0.11, 0.26, 0.47, 0.62, and 0.86 wt.% was 123.96, 126.99, 131.56, 132.82, 135.23, and 136.56 W/m²·K, respectively. Tu et al. [63] explored the impact of nanofluid concentration on heat transfer across various Reynolds numbers, yielding similar trends in their findings.

Examining the obtained results included studying the profile of the convective heat transfer coefficient in relation to the Reynolds number. While maintaining a constant nanoparticle concentration, an increase in the Reynolds number resulted in an augmentation of the heat transfer coefficient. This phenomenon can be attributed to the escalating viscosity of the nanofluid due to the addition of nanoparticles. The heightened viscosity amplified the volumetric flow rate, acting as a rationale for the increased convective heat transfer coefficient with the Reynolds number. As illustrated in Figure 7, the profile of the heat transfer coefficient exhibited more significant changes at higher Reynolds numbers compared to lower Reynolds numbers. The maximum heat transfer coefficient value was observed at a concentration of 0.86 wt.% and a Reynolds number of 480, reaching 376.23 W/m²·K. This indicated a 10.75% increase compared to the base fluid.

Preprints.org (www.preprints.org) | NOT PEER-REVIEWED | Posted: 21 August 2024 doi:10.20944/preprints202408.1412.v1

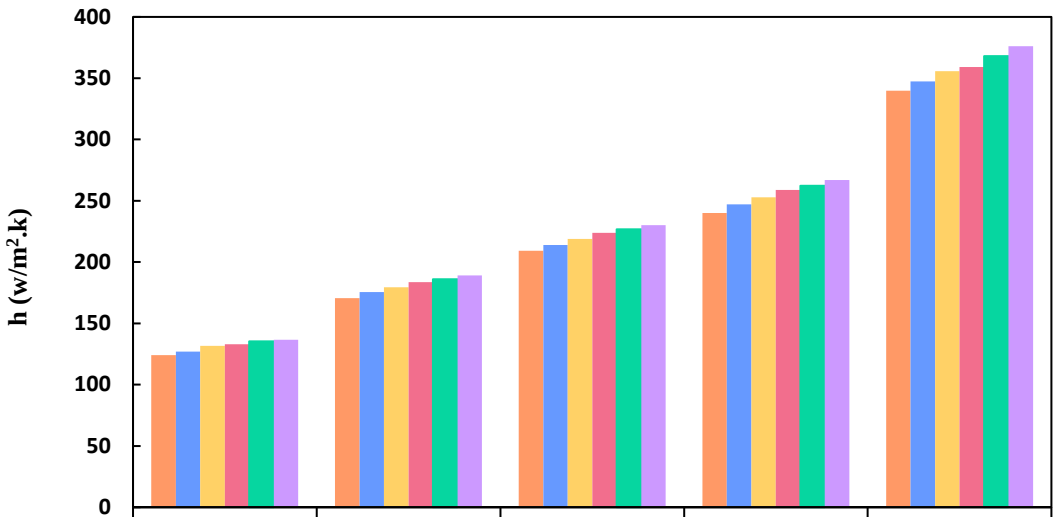

	60	120	180	240	480
0	123.96	170.62	209.31	240.12	339.71
0.11	126.99	175.44	213.85	247.11	347.36
0.26	131.56	179.47	218.77	252.84	355.63
0.47	132.82	183.54	223.88	258.79	359.11
0.62	135.23	185.85	226.75	262.14	368.07
0.86	136.56	189.22	230.093	267.02	376.23

Re

Figure 7. Variations of convection heat transfer coefficient at different Reynolds numbers and concentrations.

To enhance the comprehension of the nanoparticle's influence on the convective heat transfer coefficient, temperature contours are displayed for the highest Reynolds numbers and 0 and 0.86 wt.% concentrations in Figure 8. Increasing concentration of nanoparticles led to a reduction in the temperature of the hot surfaces, which suggested a positive impact of nanoparticles on heat transfer and cooling efficiency.

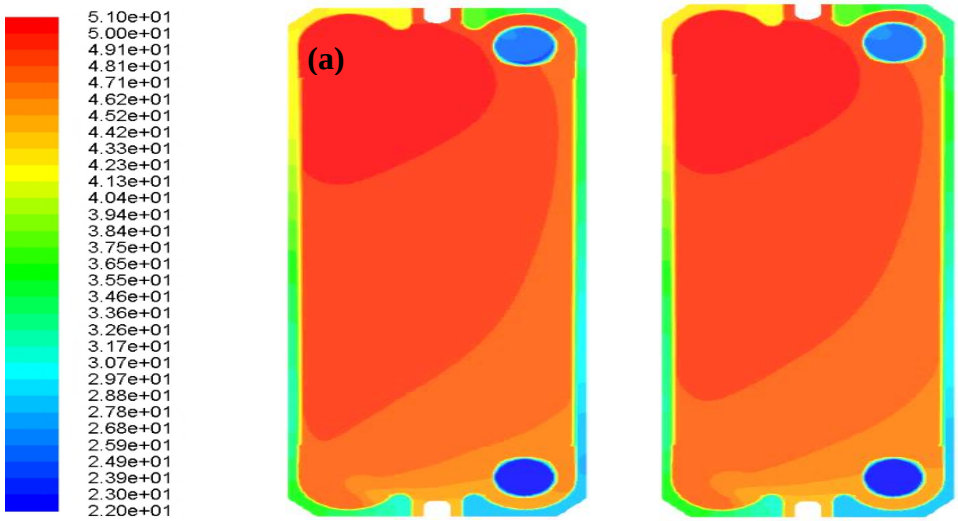

Figure 8. Contour plots of temperature variations on the hot surfaces at Re=480 and concentration of (a) 0 wt.%, and (b) 0.86 wt.%.

Pressure drop in a PHE correlates directly with the flow's Reynolds number, the thermophysical properties of the nanofluid, and the hydraulic diameter of the heat exchanger. As depicted in Figure

Preprints.org (www.preprints.org) | NOT PEER-REVIEWED | Posted: 21 August 2024 doi:10.20944/preprints202408.1412.v1

9, elevating Reynolds number resulted in a corresponding increase in the pressure drop. This relationship stems from the higher Reynolds number causing an augmentation in flow velocity within the heat exchanger channels, consequently leading to an elevation in pressure drop. Moreover, the introduction of nanoparticles resulted in heightened viscosity and subsequently increased the pressure drop. This phenomenon originated from the alteration of the base fluid's thermophysical properties upon the addition of nanoparticles. As the nanofluid concentration rose, both density and viscosity increased, contributing to an overall elevation in pressure drop along the plate heat exchanger. Consequently, this amplified the pumping power required for fluid circulation. In summary, using nanoparticles exhibited a positive influence on pressure drop. Although increasing the concentration results in more fraction which resulted in higher pressure drop, the difference was relatively marginal. For example, at a Reynolds number of 60, the pressure-drop values ranged from 37.64 Pa for the base fluid to 52.64 Pa for the highest concentration studied (0.86 wt.%). This suggested that at higher nanoparticle concentrations, the pressure drop in the plate heat exchanger did not exhibit significant variation. Mousavi et al. [64, 65] explored a similar trend and provided justification for the impact of nanoparticles on the thermophysical properties of a nanofluid with a diesel oil base.

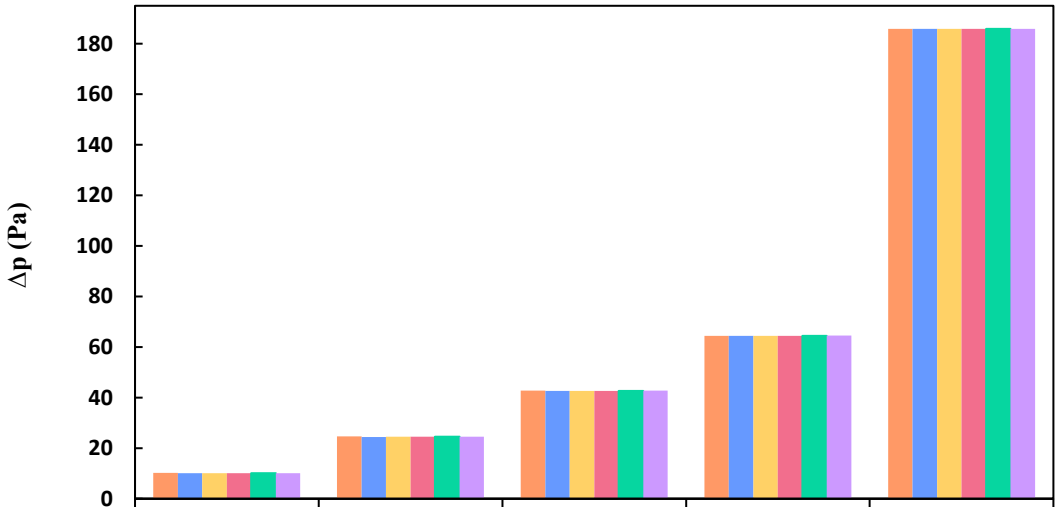

	60	120	180	240	480
0	10.17	24.64	42.74	64.37	185.92
0.11	10.08	24.46	42.61	64.39	185.91
0.26	10.11	24.48	42.63	64.41	185.89
0.47	10.11	24.51	42.67	64.45	185.87
0.62	10.13	24.53	42.70	64.48	185.85
0.86	10.13	24.57	42.74	64.52	185.83

Figure 9. Variations of pressure drop at different Reynolds numbers and concentrations.

To facilitate visual understanding, Figure 10 displays a contour plot of pressure on the hot plate for a concentration of 0.86 wt.% at all examined Reynolds numbers, accompanied by velocity vectors on both hot and cold plates. The observation revealed that elevating the Reynolds number correlates with increased velocity, ultimately resulting in an increased pressure drop across the plate.

Preprints.org (www.preprints.org) | NOT PEER-REVIEWED | Posted: 21 August 2024 doi:10.20944/preprints202408.1412.v1

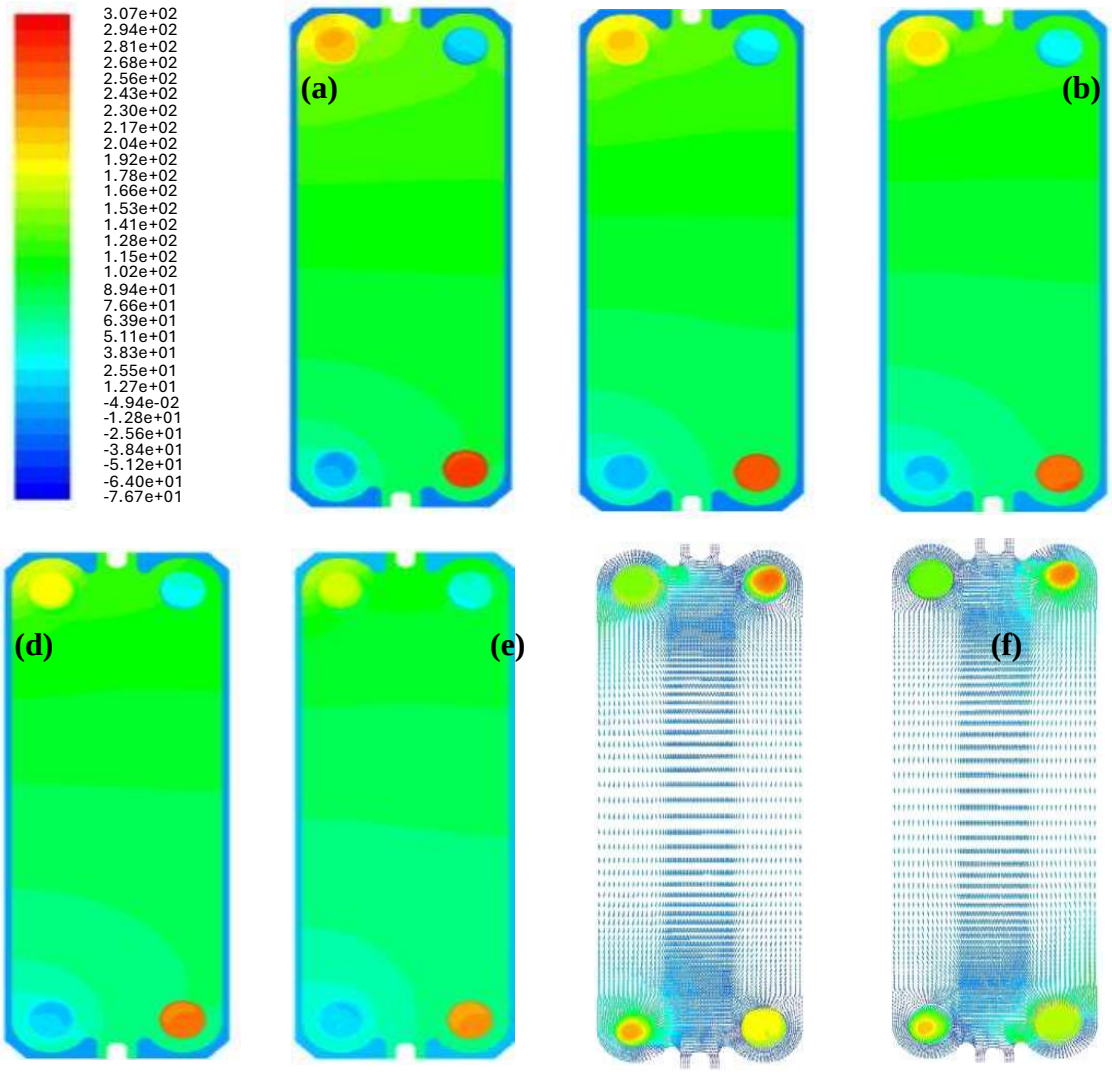

Figure 10. Contour plot of pressure on the hot plate for concentration of 0.86 wt.% at Reynolds numbers (a) 60, (b) 120, (c) 180, (d) 240, (e) 480, and velocity vectors on (f) hot, and (g) cold plates.

3.6. Single-Phase and Two-Phase States Comparison

Two general perspectives on nanofluids, namely single-phase and two-phase states, were discussed in section 2.1. In this study, we adopted the two-phase perspective, which involves a strong assumption of coupling between the two phases and mutual infiltration. This implies that each phase independently possesses its specific velocity vector field, and each control volume contains fractions of both the primary and secondary phases. Consequently, numerical simulations using the two-phase model are expected to yield more accurate results compared to the single-phase approach.

Figure 11a illustrates a comparison between Nusselt numbers for the single-phase and two-phase states at various Reynolds numbers, particularly at the highest concentration of 0.86 wt.%. Based on the achieved results, it was evident that the two-phase state provided more accurate predictions compared to the single-phase approach. The two-phase accommodates all flow parameters, including relative solid phase velocity, drag coefficient, Brownian motion of particles, and other relevant parameters in modeling, providing a more accurate relationship. As the Reynolds number increases, the distinction between the two viewpoints becomes more pronounced. This was attributed to the fact that as the Reynolds number increased, the fluid velocity rose, leading to an enhanced velocity of the secondary phase. This, in turn, intensified particle interactions and enhanced

Preprints.org (www.preprints.org) | NOT PEER-REVIEWED | Posted: 21 August 2024 doi:10.20944/preprints202408.1412.v1

heat transfer. For instance, in the mixed case, the Nusselt number at a concentration of 0.86 wt.% at Reynolds number of 60 was 11.20 and 10.57, and at Reynolds number of 480 was 34.36 and 29.120 for two-phase and single-phase, respectively. The results from both perspectives converged at lower Reynolds numbers compared to higher Reynolds numbers. This convergence may be attributed to the proximity of nanoparticle concentration at lower concentrations and intensified random particle movements with an increase in Reynolds number. As Reynolds number increased, molecular collision within the particles intensified, and the increase in secondary phase velocity led to heightened turbulence in the flow. The elaborated justifications resulted in enhancing heat transfer in the two-phase perspective. Overall, the outcomes from the two-phase method demonstrated a higher level of accuracy, with an average increase of 12.30% compared to the single-phase method and 23.974% compared to the base fluid.

For a better understanding about the impact of the two-phase perspective, a comparison was made between the convective heat transfer coefficient in single-phase and two-phase states and the results are shown in Figure 11b. As evident in the figure, the two-phase model accurately predicted the fluid flow behavior with a concentration of 0.86 wt.% compared to the single-phase model across various Reynolds numbers. Numerous factors, such as gravity, fluid-particle friction, Brownian forces, Brownian diffusion phenomenon, sedimentation, and dispersion, can interact in the fluid flow. This suggests that the slip velocity between the fluid and particles may not be zero. Therefore, the two-phase state in nanofluids provided better results compared to the single-phase, demonstrating a generally improved alignment with experimental findings [66]. The discrepancy between outcomes in the two conditions escalated with an elevation in Reynolds number. This observation was substantiated by the inclusion of the gravitational term and drag coefficient in equations 23 and 24. For Reynolds numbers below 1000, the relative velocity of the secondary phase exhibited an augmentation corresponding to the increasing Reynolds number. The velocity gradient at higher Reynolds numbers heightened Brownian motions and turbulence, subsequently amplifying the heat transfer coefficient. For instance, at Reynolds number 60, the heat transfer coefficient for the single-phase was 56.136 $W/m^2 \cdot K$, whereas in the two-phase scenario, it reached 74.144 $W/m^2 \cdot K$. In summary, the multiphase mixed perspective demonstrated superior precision compared to the single-phase condition. This was evident in an 18% elevation in Reynolds number 480 in the two-phase state compared to the single-phase state, with the highest concentration. Additionally, there was a 30.69% increase compared to the base fluid, resulting in an average percentage elevation of 12.30% compared to the single-phase state.

Figure 11c illustrates the outcomes of the identical experiment in both conditions for assessing pressure drop. The pressure drop in the two-phase state was marginally higher compared to the single-phase state which can be attributed to the formulation of the mixed two-phase. This perspective treats secondary phases, which include solid nanoparticles, as discrete entities and analyzes momentum and multiphase equations separately for each phase. In the two-phase state, the velocity of the secondary phase becomes a significant parameter distinguishing it from the single-phase state. With an increase in the Reynolds number, the total fluid velocity, relative velocity, and particle viscosity all experience an increase. Given these definitions, it can be asserted that the pressure drop in the two-phase state is slightly higher than in the single-phase state. For example, at Reynolds number 480, the pressure drop for the single-phase condition was 83.185 Pascal, whereas for the mixed two-phase scenario, it was 01.215 Pascal. In general, based on the interpretations provided, the conclusion can be drawn that the two-phase state demonstrated superior accuracy in predicting pressure drop. Specifically, at the highest Reynolds number, the increase in pressure drop in the two-phase state compared to the single-phase state and the base fluid was 35%, with an average percentage increase of 26.35%.

Preprints.org (www.preprints.org) | NOT PEER-REVIEWED | Posted: 21 August 2024 doi:10.20944/preprints202408.1412.v1

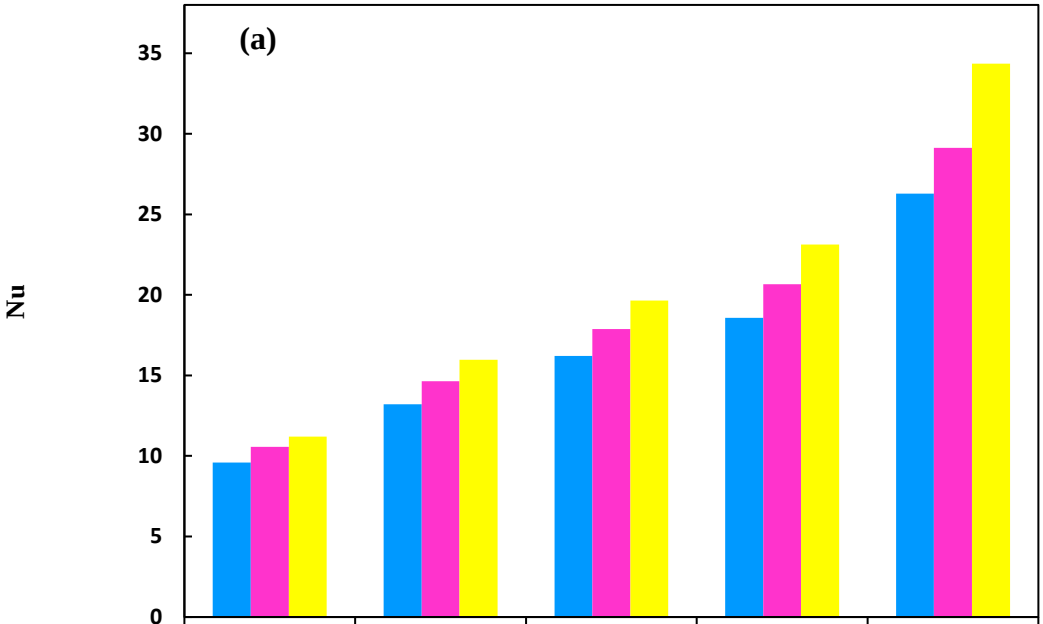

	60	120	180	240	480
EG	9.59	13.20	16.20	18.58	26.29
Single phase	10.57	14.64	17.87	20.66	29.12
Two phase	11.20	15.97	19.64	23.12	34.36

Re

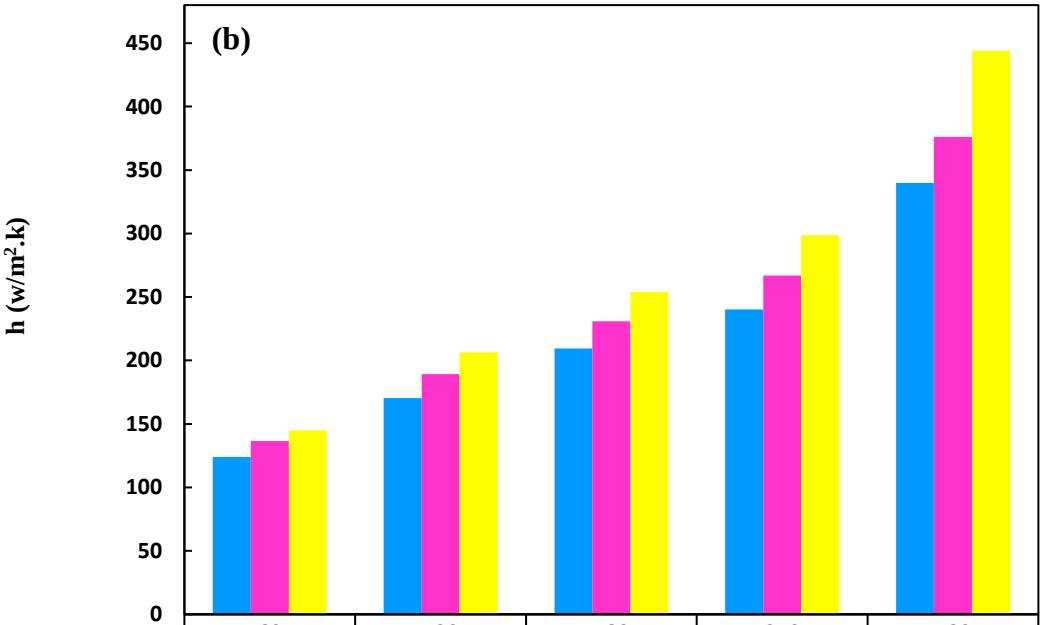

	60	120	180	240	480
EG	123.96	170.26	209.31	240.12	339.71
Single phase	136.56	189.22	230.93	267.02	376.23
Two phase	144.74	206.38	253.79	298.69	443.98

Re

Preprints.org (www.preprints.org) | NOT PEER-REVIEWED | Posted: 21 August 2024 doi:10.20944/preprints202408.1412.v1

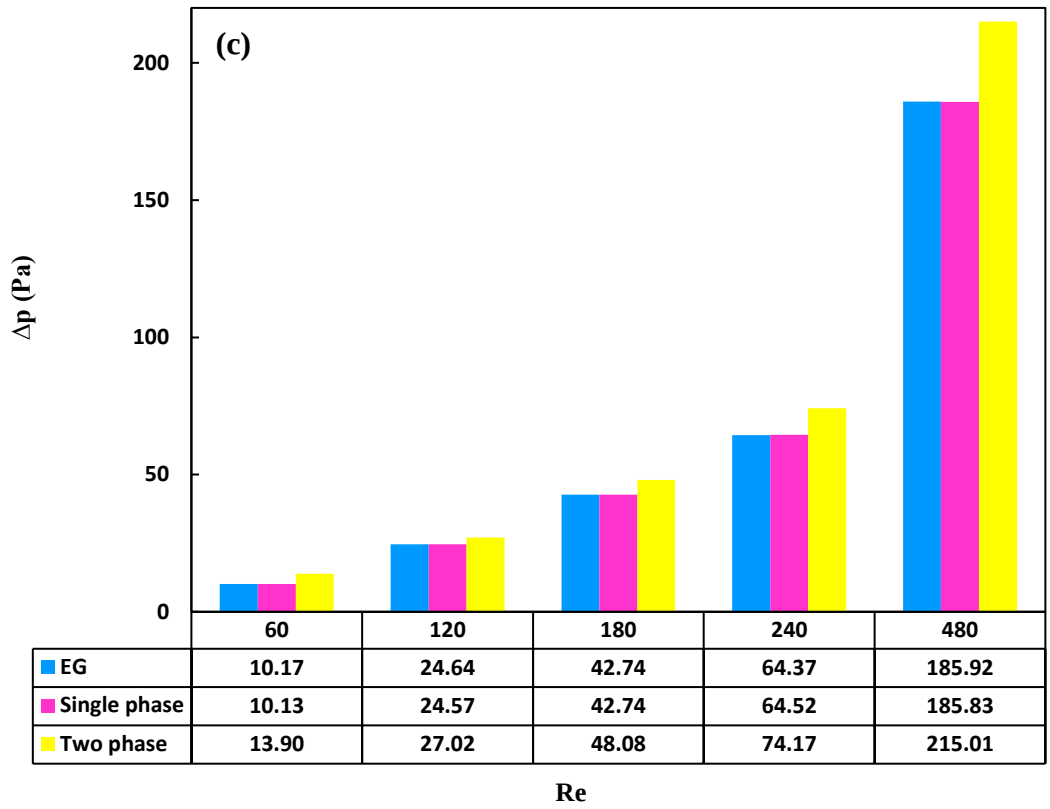

	60	120	180	240	480
EG	10.17	24.64	42.74	64.37	185.92
Single phase	10.13	24.57	42.74	64.52	185.83
Two phase	13.90	27.02	48.08	74.17	215.01

Figure 11. Variations of (a) Nusselt number, (b) convection heat transfer coefficient, and (c) pressure drop at different Reynolds numbers for base fluid and nanofluids with concentrations of 0.86 wt.% in single-phase and two-phase states.

3.7. Nano Additives Effect on Synergistic Properties

This study investigated the influence of MWCNTs on the convective heat transfer coefficient relative to hybrid and SiO_2 nanoparticles, as depicted in Figure 12a. The convective heat transfer coefficient exhibited a substantial increase in the case of hybrid nanoparticles, particularly with the incorporation of MWCNTs and SiO_2, compared to SiO_2 alone. This enhancement can be ascribed to two primary factors. Firstly, SiO_2's thermal conductivity falls within the range of 1.4 W/(m·K), whereas MWCNTs exhibit a thermal conductivity ranging from 2000 to 6000 W/(m·K), making it 1500 to 4000 times higher. Furthermore, the introduction of MWCNTs leads to the occupation of fluid space, forming a network of nanoparticle/nanotube clusters within the fluid through the attachment of SiO_2 particles to the MWCNTs. These clusters effectively mitigate thermal resistance between nanoparticles, contrasting with a nanofluid where particles are well-dispersed, resulting in heightened heat conduction. The second factor encompasses random particle movements, collisions, inter-particle interference, and velocity variations between nanoparticles and the base fluid, all contributing to the potential increase in heat transfer. As nanoparticles experience Brownian motion, they collide with each other and the surrounding fluid molecules, contributing to increased thermal energy exchange. This, in turn, facilitates a more effective transfer of heat between the nanoparticles and the fluid. Moreover, Particle collisions and inter-particle interference disrupt the fluid flow patterns, creating localized turbulence and enhancing convective heat transfer. This increased turbulence facilitates better mixing of the fluid, promoting efficient heat distribution across the system. Variations in velocity between nanoparticles and the base fluid result in dynamic fluid flow patterns, creating regions of higher and lower temperature. These temperature variations contribute to convective currents, promoting heat transfer and distribution throughout the fluid.

The research objective was to substantiate the positive impact of MWCNTs on heat transfer at a constant Reynolds number, particularly with an increasing concentration. The obtained results clearly indicated that addition of the concentration of hybrid nanoparticles led to an improved

Preprints.org (www.preprints.org) | NOT PEER-REVIEWED | Posted: 21 August 2024 doi:10.20944/preprints202408.1412.v1

convective heat transfer coefficient. At the highest concentration, the addition of MWCNTs positively contributed to the convective heat transfer coefficient by 9.28%, 8.41%, and 10.75% compared to hybrid nanoparticles, SiO_2, and EG, respectively.

The impact of incorporating MWCNTs into hybrid nanoparticles on pressure drop is depicted in Figure 12b. Pressure drop is influenced by factors such as thermophysical properties, fluid velocity, and the geometric configuration of the specific plate heat exchanger in consideration. Despite the addition of a new particle and an increase in viscosity, it was observed that the pressure drop of the hybrid nanoparticle was slightly lower than that of SiO_2 nanoparticles. The reduction in pressure drop can be ascribed to the density of the associated particles. SiO_2 has a volumetric mass of 2600 kg/m³, whereas MWCNTs have a volumetric mass of 1200 kg/m³. Consequently, the pressure drop in the singular case was higher compared to the hybrid case. Under the highest achievable conditions (Reynolds number of 480 and concentration of 0.86 wt.%), SiO_2 nanoparticles exhibited a marginal increase (0.06%) in pressure drop compared to hybrid nanoparticles. This minor increment suggests that the addition of MWCNTs does not significantly contribute to pressure drop in the heat exchanger.

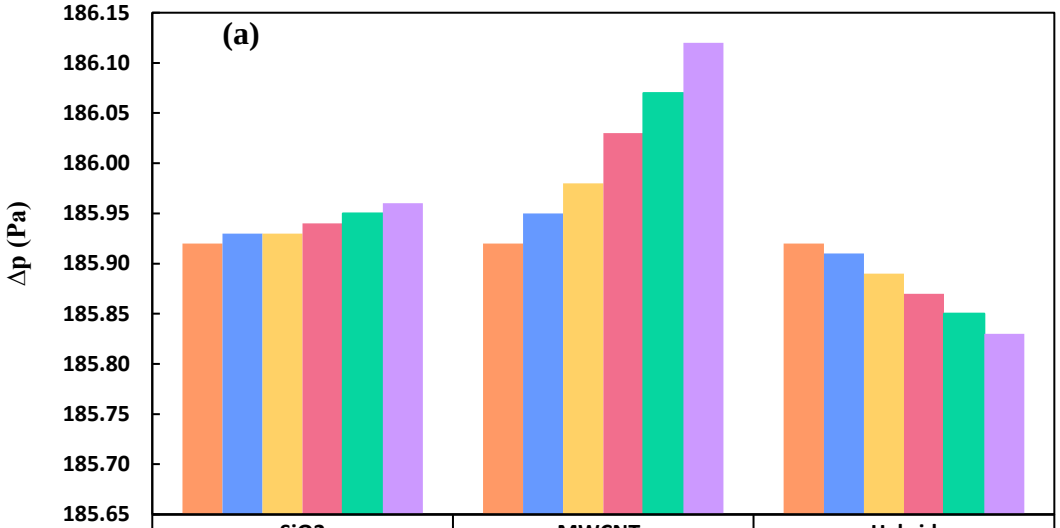

	SiO2	MWCNTs	Hybrid
0	185.92	185.92	185.92
0.11	185.93	185.95	185.91
0.26	185.93	185.98	185.89
0.47	185.94	186.03	185.87
0.62	185.95	186.07	185.85
0.86	185.96	186.12	185.83

Preprints.org (www.preprints.org) | NOT PEER-REVIEWED | Posted: 21 August 2024 doi:10.20944/preprints202408.1412.v1

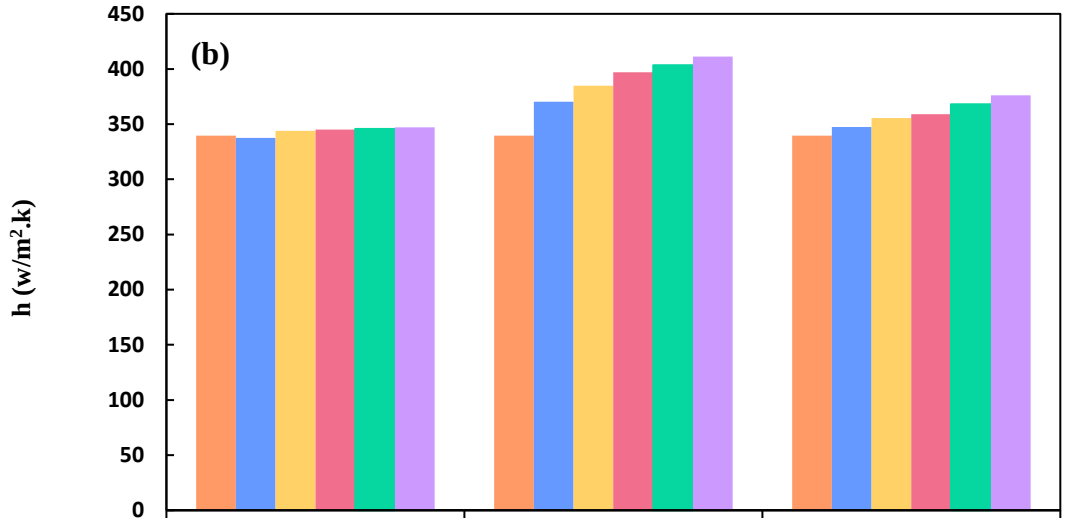

	SiO2	MWCNTs	Hybrid
0	339.71	339.71	339.71
0.11	337.60	370.31	347.36
0.26	343.88	384.89	355.63
0.47	344.99	397.05	359.11
0.62	345.77	403.32	368.07
0.86	347.04	411.15	376.23

Figure 12. Variations of (a) convection heat transfer coefficient, and (b) pressure drop at Re=480 for nanofluids at different concentrations.

The incorporation of MWCNTs, hybrid, and SiO_2 nano-additives yielded improvements in the heat transfer coefficient by 21.02%, 10.76%, and 2.16%, respectively. Simultaneously, the introduction of MWCNTs, hybrid, and SiO_2 nano-additives brought about corresponding adjustments in pressure difference by 0.11%, 0.04%, and 0.02%, respectively. MWCNTs demonstrated the most favorable heat transfer coefficient but the least desirable pressure drop, whereas SiO_2 exhibited the least favorable heat transfer coefficient but the most favorable pressure drop. The impact on convective heat transfer coefficients with MWCNTs was 5-10% higher than that observed with the hybrid additives. Notably, the introduction of MWCNTs resulted in increased pressure, while the hybrid additives led to a decrease in pressure due to cluster formation. In summary, the hybrid additive demonstrated the optimal enhancement in heat transfer coefficient and yielded favorable pressure drop outcomes. The cost-effectiveness and adaptability inherent in hybrid nanoparticles, with their synergistic material combinations, position them as promising solutions to overcome specific challenges in cooling technologies. The combination of various materials within hybrid nanoparticles results in synergistic effects, endowing them with properties superior to those of individual components. This synergy translates into enhanced overall performance, increased stability, and improved functionality, making hybrid nanoparticles a compelling choice for diverse cooling applications. Moreover, their tailored functionality and adaptability contribute significantly to elevated thermal management in different industrial sectors.

4. Conclusions and Future Considerations

This study concentrated on employing computational fluid dynamics to simulate a PHE and examine the impact of SiO_2, MWCNTs, and their hybrid combination in an EG base fluid. Additionally, it compared and analyzed two scenarios: single-phase and two-phase (mixture model). The ensuing results can be summarized as follows:

Preprints.org (www.preprints.org) | NOT PEER-REVIEWED | Posted: 21 August 2024 doi:10.20944/preprints202408.1412.v1

1. The findings indicated that the convective heat coefficient rose in tandem with both the Reynolds number and nanoparticle concentration. Notably, the study identified a peak enhancement of 10.76% in the heat transfer coefficient when hybrid nano additives were incorporated at 0.86 wt.%, resulting in a value of 376.23 W/(m^2·K).
2. The addition of nanoparticles to the base fluid has generally resulted in an increase in the viscosity and density of the base fluid, accompanied by a corresponding rise in the overall pressure drop. It is noteworthy that the nanofluid, even at its highest concentration (0.86 wt.%), experienced a minimal pressure drop in both the inlet and outlet channels, highlighting one of the advantageous aspects of used nano additives.
3. Upon comparing the results obtained for the single-phase and two-phase states, it was evident that the two-phase configuration demonstrated superior accuracy in contrast to both the single-phase state and the base fluid.
4. Comparing the hybrid nanoparticles with SiO_2 nanoparticles and MWCNTs revealed that incorporating MWCNTs increased the heat transfer coefficient and decreased the pressure drop. Moreover, MWCNTs exhibited the highest convective heat transfer coefficient among the scenarios; however, MWCNTs had only values that were 5-10% more than hybrid. Hybrid nanoparticles resulted in a pressure drop by 0.04% while DWCNT and SiO_2 increased the pressure by 0.11% and 0.02%, respectively. The pressure for hybrid nanoparticles was the lowest when contrasted with single nanoparticles, showcasing a well-supported synergistic effect.
5. The hybrid nanoparticles under consideration proved to be highly effective in the PHE, indicating their potential applicability across a spectrum of industries. This versatility extends to cooling systems, computer setups, and engine cooling, where these nanoparticles exhibit notable performance as efficient coolants.

Different heat exchanger geometries may yield varying results. Future research should focus on comprehensive experimental studies across broader nanoparticle loadings and flow conditions. Exploring synergies with other nanoparticle combinations and surface functionalization could improve performance further. Investigating long-term stability, fouling tendencies, economic feasibility, and environmental implications would also be crucial for practical implementation of hybrid nanofluid-based cooling systems.

Preprints.org (www.preprints.org) | NOT PEER-REVIEWED | Posted: 21 August 2024 doi:10.20944/preprints202408.1412.v1

Author Contributions: Saeed Zeinali Heris: Supervision, Conceptualization, Methodology, Validation. Nima Zolfagharian: Investigation. Seyed Borhan Mousavi: Formal analysis, Writing original draft. Shamin Hosseini Nami: Formal analysis, Writing original draft.

Funding: This research did not receive any specific funding.

Data Availability: All data generated or analysed during this study are included in this published article.

Declaration of Competing Interest: The authors declare that they have no known competing financial interests or personal relationships that could have appeared to influence the work reported in this paper.

Nomenclature

Acceleration (m/s^2)	α
Depth of plates (mm)	b_c
Specific heat of the fluid (J/kg K)	C_P
Channel diameter (mm)	D
Drag function	f_{drag}
Gravity acceleration (m/s^2)	g
Enthalpy (J/kg)	H
Thermal conductivity (W/m K)	K
Reynolds number	Re
Temperature (K)	T/t
Velocity (m/s)	V/v
Number of plates	N
Pressure (Pa)	P
Fluctuating pressure	$\acute{p}$
Mean pressure	$\bar{p}$
Thickness of plates (mm)	t
Mean velocity	$\bar{u}$
Fluctuating velocity	u'
Width of plates (mm)	w
Turbulent kinetic energy	k
Greek letters	
Plate area enlargement factor	ϕ
Particle concentration	φ
Thermal conductivity of the fluid (W/mK)	λ
Fluid dynamic viscosity (kg/m s)	μ

Preprints.org (www.preprints.org) | NOT PEER-REVIEWED | Posted: 21 August 2024 doi:10.20944/preprints202408.1412.v1

Fluid density (kg/m^3)	ρ
Shear stress (Pa)	τ
Shear rate (1/s)	γ
Subscripts	
Base fluid	bf
Primary phase	f
Hybrid nanofluid	hnf
kth phase	k
Mixture	m
Nanofluid	nf
Particle property	p
Nanofluid/base fluid ratio	R
Turbulent	t
Equivalent	e

References

1. 1. Dharmakkan N, Srinivasan PM, Muthusamy S, Jomde A, Shamkuwar S, Sonawane C et al. A case study on analyzing the performance of microplate heat exchanger using nanofluids at different flow rates and temperatures. Case Studies in Thermal Engineering. 2023;44:102805.
2. 2. Goshayeshi HR, Mousavi SB, Heris SZ, Chaer I. Insights into two-phase flow dynamics in closed-loop pulsating heat pipes utilizing Fe3O4/water: experimental visualization study. Scientific Reports. 2024;14(1):16497.
3. 3. Porgar S, Oztop HF, Salehfekr S. A comprehensive review on thermal conductivity and viscosity of nanofluids and their application in heat exchangers. Journal of Molecular Liquids. 2023:122213.
4. 4. Karimi Shoar Z, Pourpasha H, Zeinali Heris S, Mousavi SB, Mohammadpourfard M. The effect of heat transfer characteristics of macromolecule fouling on heat exchanger surface: A dynamic simulation study. The Canadian Journal of Chemical Engineering. 2023;101(10):5802-17.
5. 5. Sriharan G, Harikrishnan S, Oztop HF. Performance improvement of the mini hexagonal tube heat sink using nanofluids. Thermal Science and Engineering Progress. 2022;34:101390.
6. 6. Bayrak F, Oztop HF, Selimefendigil F. Experimental study for the application of different cooling techniques in photovoltaic (PV) panels. Energy Conversion and Management. 2020;212:112789.
7. 7. Porgar S, Rahmanian N. Investigation of Effect of Aluminium Oxide Nanoparticles on the Thermal Properties of Water-Based Fluids in a Double Tube Heat Exchanger. 2021.
8. 8. Khalifa AJN, Banwan MA. Effect of volume fraction of γ-Al2O3 nanofluid on heat transfer enhancement in a concentric tube heat exchanger. Heat Transfer Engineering. 2015;36(16):1387-96.
9. 9. Zheng D, Wang J, Chen Z, Baleta J, Sundén B. Performance analysis of a plate heat exchanger using various nanofluids. International Journal of Heat and Mass Transfer. 2020;158:119993.
10. 10. Ajeeb W, da Silva RRT, Murshed SS. Experimental investigation of heat transfer performance of Al2O3 nanofluids in a compact plate heat exchanger. Applied Thermal Engineering. 2023;218:119321.
11. 11. Heris SZ, Bagheri H, Mousavi SB, Hosseini Nami S. Optimizing nanofluid additives for enhanced thermophysical properties in anionic crude oil for EOR applications. The Canadian Journal of Chemical Engineering. 2024.
12. 12. Heris SZ, Ebadiyan H, Mousavi SB, Nami SH, Mohammadpourfard M. The influence of nano filter elements on pressure drop and pollutant elimination efficiency in town border stations. Scientific Reports. 2023;13(1):18793.
13. 13. Ashrafivala M, Mousavi SB, Heris SZ, Heidari M, Mohammadpourfard M, Aslani H. Investigation of H2O2/UV advanced oxidation process on the removal rate of coliforms from the industrial effluent: A pilot-scale study. International Journal of Hydrogen Energy. 2022;47(78):33530-40.

Preprints.org (www.preprints.org) | NOT PEER-REVIEWED | Posted: 21 August 2024 doi:10.20944/preprints202408.1412.v1

14. 14. Ebadiyan H, Heris SZ, Mousavi SB, Nami SH, Mohammadpourfard M. The influence of nano filter elements on pressure drop and pollutant elimination efficiency in town border stations. Scientific Reports. 2023;13(1):18793.
15. 15. Heidari M, Mousavi SB, Rahmani F, Aminabhavi TM, Rezakazemi M. Insightful textural/morphological evaluation of cost-effective and highly sustainable Ca-Zr-O nanosorbent modified with the waste date kernel as a biomass pore-former for high-temperature CO2 capture. Sustainable Materials and Technologies. 2023;38:e00778.
16. 16. Heidari M, Mousavi SB, Rahmani F, Clough PT, Ozmen S. The novel Carbon Nanotube-assisted development of highly porous CaZrO3-CaO xerogel with boosted sorption activity towards high-temperature cyclic CO2 capture. Energy Conversion and Management. 2022;274:116461.
17. 17. Heidari M, Mousavi SB, Rahmani F, Sene RA. Eco-friendly, sustainable and porous eggshell/tea waste-derived CaO nanoparticles as a high-temperature CO2 sorbent: Fabrication and textural/morphological evaluation. Journal of Industrial and Engineering Chemistry. 2024;134:169-80.
18. 18. Heidari M, Tahmasebpoor M, Mousavi SB, Pevida C. CO2 capture activity of a novel CaO adsorbent stabilized with (ZrO2+ Al2O3+ CeO2)-based additive under mild and realistic calcium looping conditions. Journal of CO2 Utilization. 2021;53:101747.
19. 19. Hosseini Nami S, Mousavi SB. Nitrate removal performance of different granular adsorbents using a novel fe-exchanged nanoporous clinoptilolite. Industrial & Engineering Chemistry Research. 2023;62(8):3659-71.
20. 20. Jalaie A, Afshaar A, Mousavi SB, Heidari M. Investigation of the Release Rate of Biocide and Corrosion Resistance of Vinyl-, Acrylic-, and Epoxy-Based Antifouling Paints on Steel in Marine Infrastructures. Polymers. 2023;15(19):3948.
21. 21. Mousavi SB, Heidari M, Rahmani F, Sene RA, Clough PT, Ozmen S. Highly robust ZrO2-stabilized CaO nanoadsorbent prepared via a facile one-pot MWCNT-template method for CO2 capture under realistic calcium looping conditions. Journal of Cleaner Production. 2023;384:135579.
22. 22. Naghash-Hamed S, Arsalani N, Mousavi SB. Facile copper ferrite/carbon quantum dot magnetic nanocomposite as an effective nanocatalyst for reduction of para-nitroaniline and ortho-nitroaniline. Nano Futures. 2022;6(4):045003.
23. 23. Naghash-Hamed S, Arsalani N, Mousavi SB. The catalytic performance of CuFe2O4@ CQD nanocomposite as a high-perform heterogeneous nanocatalyst in nitroaniline group reduction. Scientific Reports. 2023;13(1):3329.
24. 24. Sobhani E, Heris SZ, Mousavi SB. The synergistic effect of intumescent fire-resistive paint containing TiO2 nanoparticles and chlorinated paraffin onto atmospheric-metallic substrates. ChemistrySelect. 2022;7(44):e202203513.
25. 25. Seyedi SS, Shabgard MR, Mousavi SB, Heris SZ. The impact of SiC, Al2O3, and B2O3 abrasive particles and temperature on wear characteristics of 18Ni (300) maraging steel in abrasive flow machining (AFM). International Journal of Hydrogen Energy. 2021;46(68):33991-4001.
26. 26. Heris SZ, Etemadi M, Mousavi SB, Mohammadpourfard M, Ramavandi B. Preparation and characterizations of TiO2/ZnO nanohybrid and its application in photocatalytic degradation of tetracycline in wastewater. Journal of Photochemistry and Photobiology A: Chemistry. 2023;443:114893.
27. 27. Yousefi F, Mousavi SB, Heris SZ, Naghash-Hamed S. UV-shielding properties of a cost-effective hybrid PMMA-based thin film coatings using TiO2 and ZnO nanoparticles: a comprehensive evaluation. Scientific Reports. 2023;13(1):7116.
28. 28. Naghash-Hamed S, Arsalani N, Mousavi SB. Facile fabrication of CuFe2O4 coated with Carbon Quantum Dots nanocomposite as an efficient heterogeneous catalyst toward the reduction of nitroaniline compounds for management of aquatic resources. Journal of Photochemistry and Photobiology A: Chemistry. 2023;443:114822.
29. 29. Naghash-Hamed S, Arsalani N, Mousavi SB. The catalytic reduction of nitroanilines using synthesized CuFe2O4 nanoparticles in an aqueous medium. ChemistryOpen. 2022;11(11):e202200156.
30. 30. Gupta SK, Gupta S, Gupta T, Raghav A, Singh A. A review on recent advances and applications of nanofluids in plate heat exchanger. Materials Today: Proceedings. 2021;44:229-41.
31. 31. Pourpasha H, Heris SZ, Mousavi SB. Thermal performance of novel ZnFe2O4 and TiO2-doped MWCNT nanocomposites in transformer oil. Journal of Molecular Liquids. 2024;394:123727.
32. 32. Sundar LS. Synthesis and characterization of hybrid nanofluids and their usage in different heat exchangers for an improved heat transfer rates: A critical review. Engineering Science and Technology, an International Journal. 2023;44:101468.
33. 33. Alklaibi A, Mouli KVC, Sundar LS. Heat transfer, and friction factor of Fe3O4–SiO2/water hybrid nanofluids in a plate heat exchanger: experimental and ANN predictions. International Journal of Thermal Sciences. 2024;195:108608.

Preprints.org (www.preprints.org) | NOT PEER-REVIEWED | Posted: 21 August 2024 doi:10.20944/preprints202408.1412.v1

34. 34. Abidi A, Sajadi SM. Numerical assessment of hydraulic behavior and thermal efficiency of multiphase hybrid nanofluid in a shell-and-tube heat exchanger with inclined baffles. Engineering Analysis with Boundary Elements. 2023;156:114-25.
35. 35. Bhattad A. Better performance criteria for plate heat exchanger with hybrid nanofluid: flow rate or concentration. Journal of Thermal Analysis and Calorimetry. 2023;148(24):14295-304.
36. 36. Bhattad A, Sarkar J, Ghosh P. Experimentation on effect of particle ratio on hydrothermal performance of plate heat exchanger using hybrid nanofluid. Applied Thermal Engineering. 2019;162:114309.
37. 37. Sundar LS, Mouli KVC. Effectiveness and number of transfer units of plate heat exchanger with Fe3O4–SiO2/Water hybrid nanofluids: Experimental and artificial neural network predictions. Case Studies in Thermal Engineering. 2024;53:103949.
38. 38. Afshari F, Tuncer AD, Sözen A, Variyenli HI, Khanlari A, Gürbüz EY. A comprehensive survey on utilization of hybrid nanofluid in plate heat exchanger with various number of plates. International Journal of Numerical Methods for Heat & Fluid Flow. 2022;32(1):241-64.
39. 39. . https://www.alfalaval.sg/products/heat-transfer/plate-heat-exchangers/gasketed-plate-and-frame-heat-exchangers/heat-exchanger/how-plate-heat-exchanger-work/.
40. 40. Islam MS, Saha SC. Heat transfer enhancement investigation in a novel flat plate heat exchanger. International Journal of Thermal Sciences. 2021;161:106763.
41. 41. Huang D, Wu Z, Sunden B. Pressure drop and convective heat transfer of Al2O3/water and MWCNT/water nanofluids in a chevron plate heat exchanger. International journal of heat and mass transfer. 2015;89:620-6.
42. 42. Mousavi SB, Pourpasha H, Heris SZ. High-temperature lubricity and physicochemical behaviors of synthesized Cu/TiO2/MnO2-doped GO nanocomposite in high-viscosity index synthetic biodegradable PAO oil. International Communications in Heat and Mass Transfer. 2024;156:107642.
43. 43. Khouri O, Goshayeshi HR, Mousavi SB, Hosseini Nami S, Zeinali Heris S. Heat Transfer Enhancement in Industrial Heat Exchangers Using Graphene Oxide Nanofluids. ACS omega. 2024.
44. 44. Mousavi SB, Heris SZ. Experimental investigation of ZnO nanoparticles effects on thermophysical and tribological properties of diesel oil. International Journal of Hydrogen Energy. 2020;45(43):23603-14.
45. 45. Mousavi SB, Heris SZ, Hosseini MG. Experimental investigation of MoS2/diesel oil nanofluid thermophysical and rheological properties. International Communications in Heat and Mass Transfer. 2019;108:104298.
46. 46. Javadpour R, Heris SZ, Mohammadfam Y, Mousavi SB. Optimizing the heat transfer characteristics of MWCNTs and TiO2 water-based nanofluids through a novel designed pilot-scale setup. Scientific Reports. 2022;12(1):15154.
47. 47. Mousavi S, Heris S, Estellé P. Experimental comparison between ZnO and MoS2 nanoparticles as additives on performance of diesel oil-based nano lubricant. Sci Rep 10: 5813. 2020.
48. 48. Bianco V, Manca O, Nardini S. Numerical investigation on nanofluids turbulent convection heat transfer inside a circular tube. International Journal of Thermal Sciences. 2011;50(3):341-9.
49. 49. Manninen M, Taivassalo V, Kallio S. On the mixture model for multiphase flow. 1996.
50. 50. Schiller L. A drag coefficient correlation. Zeit Ver Deutsch Ing. 1933;77:318-20.
51. 51. Sarvari AA, Heris SZ, Mohammadpourfard M, Mousavi SB, Estellé P. Numerical investigation of TiO2 and MWCNTs turbine meter oil nanofluids: Flow and hydrodynamic properties. Fuel. 2022;320:123943.
52. 52. Hemmat Esfe M, Esfandeh S, Rejvani M. Modeling of thermal conductivity of MWCNT-SiO 2 (30: 70%)/EG hybrid nanofluid, sensitivity analyzing and cost performance for industrial applications: An experimental based study. Journal of Thermal Analysis and Calorimetry. 2018;131:1437-47.
53. 53. Eshgarf H, Sina N, Esfe MH, Izadi F, Afrand M. Prediction of rheological behavior of MWCNTs–SiO 2/EG–water non-Newtonian hybrid nanofluid by designing new correlations and optimal artificial neural networks. Journal of Thermal Analysis and Calorimetry. 2018;132:1029-38.
54. 54. Pak BC, Cho YI. Hydrodynamic and heat transfer study of dispersed fluids with submicron metallic oxide particles. Experimental Heat Transfer an International Journal. 1998;11(2):151-70.
55. 55. Takabi B, Salehi S. Augmentation of the heat transfer performance of a sinusoidal corrugated enclosure by employing hybrid nanofluid. Advances in Mechanical Engineering. 2014;6:147059.
56. 56. Ghazanfari V, Imani M, Shadman MM, Amini Y, Zahakifar F. Numerical study on the thermal performance of the shell and tube heat exchanger using twisted tubes and Al2O3 nanoparticles. Progress in Nuclear Energy. 2023;155:104526.
57. 57. Shaheed R, Mohammadian A, Kheirkhah Gildeh H. A comparison of standard k–ε and realizable k–ε turbulence models in curved and confluent channels. Environmental Fluid Mechanics. 2019;19(2):543-68. doi:10.1007/s10652-018-9637-1.
58. 58. Incropera FP, DeWitt DP, Bergman TL, Lavine AS. Fundamentals of heat and mass transfer. Wiley New York; 1996.

Preprints.org (www.preprints.org) | NOT PEER-REVIEWED | Posted: 21 August 2024 doi:10.20944/preprints202408.1412.v1

59. 59. Talib S, Azmi W, Zakaria I, Mohamed W, Mamat A, Ismail H et al. Thermophysical properties of silicon dioxide (SiO2) in ethylene glycol/water mixture for proton exchange membrane fuel cell cooling application. Energy Procedia. 2015;79:366-71.
60. 60. Isa Abbasi SZH. Experimental study of the performance of a plate heat exchanger using carboxyl multi–walled carbon nanotube/water and hydroxyl multi–walled carbon nanotube/water nanofluids: University of Tabriz; 2023.
61. 61. Bazdar H, Toghraie D, Pourfattah F, Akbari OA, Nguyen HM, Asadi A. Numerical investigation of turbulent flow and heat transfer of nanofluid inside a wavy microchannel with different wavelengths. Journal of Thermal Analysis and calorimetry. 2020;139:2365-80.
62. 62. Izadi M, Alshehri HM, Hosseinzadeh F, Rad MS, Hamida MBB. Numerical study on forced convection heat transfer of TiO2/water nanofluid flow inside a double-pipe heat exchanger with spindle-shaped turbulators. Engineering Analysis with Boundary Elements. 2023;150:612-23.
63. 63. Tu J, Qi C, Li K, Tang Z. Numerical analysis of flow and heat characteristic around micro-ribbed tube in heat exchanger system. Powder Technology. 2022;395:562-83.
64. 64. Mousavi SB, Heris SZ, Estellé P. Experimental comparison between ZnO and MoS2 nanoparticles as additives on performance of diesel oil-based nano lubricant. Scientific reports. 2020;10(1):5813.
65. 65. Mousavi SB, Zeinali Heris S, Estellé P. Viscosity, tribological and physicochemical features of ZnO and MoS2 diesel oil-based nanofluids: An experimental study. Fuel. 2021;293:120481. doi:https://doi.org/10.1016/j.fuel.2021.120481.
66. 66. Mirmasoumi S, Behzadmehr A. Numerical study of laminar mixed convection of a nanofluid in a horizontal tube using two-phase mixture model. Applied Thermal Engineering. 2008;28(7):717-27.

Disclaimer/Publisher's Note: The statements, opinions and data contained in all publications are solely those of the individual author(s) and contributor(s) and not of MDPI and/or the editor(s). MDPI and/or the editor(s) disclaim responsibility for any injury to people or property resulting from any ideas, methods, instructions or products referred to in the content.